Fermi National Accelerator Laboratory

FERMILAB-Pub-90/145-A
July 1990

The Shock Process and Light Element Production in Supernovae Envelopes

LAWRENCE E. BROWN,[1,2] DAVID S. DEARBORN,[3] DAVID N. SCHRAMM,[1,2] JON T. LARSEN,[4] AND SHIN KUROKAWA[1]

[1] *University of Chicago, Chicago IL 60637-1433*

[2] *NASA/Fermilab Astrophysics Center, Fermi National Accelerator Laboratory, Batavia, IL 60510-0500*

[3] *Lawrence Livermore National Laboratories, Livermore, CA 94551*

[4] *Cascade Applied Sciences, Box 4477, Boulder, CO 80306*

Operated by Universities Research Association Inc. under contract with the United States Department of Energy

ABSTRACT

Detailed hydrodynamic modeling of the passage of supernova shocks through the hydrogen envelopes of blue and red progenitor stars has been carried out to explore the sensitivity to model conditions of light element production (specifically ^7Li and ^{11}B) which was noted by Dearborn, Schramm, Steigman and Truran (1989) (DSST). It is found that, for stellar models with $M \lesssim 100 M_\odot$, current state of the art supernova shocks do not produce significant light element yields by hydrodynamic processes alone. The dependence of this conclusion on stellar models and on shock strengths is explored. Preliminary implications for Galactic evolution of lithium are discussed, and it is suspected that intermediate mass red giant stars may be the most consistent production site for lithium.

Introduction

In recent years, lithium has become a very important probe of cosmological and Galactic history. As we will see, lithium yields are very sensitive to nucleosynthetic conditions. Small changes in the environmental parameters can lead to large changes in the amount of lithium produced or destroyed by these processes. Because of this, it has become common to try to enhance our understanding of stellar and early Universe physics by using current lithium abundances to set limits on such astrophysical parameters as the average mass density in baryons of the Universe (Kawano, Schramm, and Steigman 1988) and the depth of convection zones in proto-stars (D'Antona and Mazzitelli 1984). A big uncertainty in this approach is that there are at least two distinct abundance measurements for ^7Li . The abundance of ^7Li in low metallicity, Population II main sequence stars in the Galactic halo is constant above a certain effective stellar temperature, with an observed (Spite and Spite (1982)) ^7Li $/H$ ratio of 10^{-10}. Since the metals are assumed to have been produced as the Galaxy evolved and developed a disk, this group of stars is generally believed to be the earliest group of observed stars to have formed . This essentially constant value of the lithium abundance, over a small (but significant) range of stellar masses (all but the least massive pop II stars have long since left the main sequence) and a wide range of metallicities, has reinforced the conclusion that this lithium abundance is primordial. This is consistent with standard big bang nucleosynthesis (BBN). However, the high

metallicity ($z > .01$) stars of the Galactic disk have a consistent flat upper limit (Boesgaard 1990) of $^7Li\ /H \lesssim 10^{-9}$. This maximum abundance remains high even for the oldest pop I clusters (*e.g.* NGC188) (Hobbs and Pilachowski 1988). Thus it appears that ^7Li abundances grew along with the other heavier elements to some extent.

In general, any changes in the early Universe scenario can only make the predicted primordial lithium abundance go up. This is because lithium is formed by two different nuclear processes: either as beryllium at high densities (via $^3He(\alpha,\gamma)^7Be$) which then decays to lithium by electron capture with a lifetime of about forty-nine days, or as lithium directly (via $^4He(\alpha,p)^7Li$) at low densities. The reason that ^7Li can only be made directly at low densities is that it is very easily destroyed by the $^7Li(p,\alpha)^4He$ reaction at what are relatively low temperatures ($\sim 2 \times 10^6\ ^\circ K$) due to the extreme stability of ^4He . (At stellar densities, lithium is rapidly destroyed, at temperatures above $10^6\ ^\circ K$. ^7Be on the other hand, cannot be destroyed by protons at temperatures high enough to create it, due to photo-disintegration reactions (see below)). The gap between these two cosmological production regimes causes a dip in the lithium abundance versus density of the Universe curve (figure 1). The standard BBN abundance brackets the bottom of the dip at $Li^7/H \approx 10^{-10}$. All other theories of primordial nucleosynthesis (for example inhomogeneous nucleosynthesis (Applegate, Hogan, and Scherrer 1987) or late decaying particle nucleosynthesis (Dimopoulus, et. al. 1988) predict higher primordial values of lithium than this, since any change in conditions will favor one or the other production mechanism to a greater degree than the standard scenario and this will cause a greater primordial ^7Li yield.

If the pop II abundance is primordial, then we need to make $\sim$ 10 times our starting abundance in some Galactic process by the time of the formation of the earliest pop I clusters. Since making lithium directly at stellar densities is impossible (any temperature hot enough to make ^7Li will immediately destroy it at a higher rate), any stellar lithium production process must follow the Cameron-Fowler (1971) paradigm of making ^7Be in a hot environment and then cooling it before the $\sim$ 49 day half-life runs out. The original Cameron-Fowler proposal used a convective red giant envelope as the production site. However,

DSST noted that similar conditions might also be achieved in supernovae. Since supernovae are by far the most theoretically favored sources of the metals, it seems reasonable that they might also be the sources of the ^7Li . This would explain why the ^7Li abundance "tracks" the metal abundance. The traditional Cameron-Fowler (1971) site of red giants and/or the alternative of classical novae (Starrfield, Truran, Sparks, and Arnould (1988)) might have difficulties explaining the pop I ^7Li abundance observed in the oldest pop I clusters because these sites involve lower mass stars which have longer lifetimes, and therefore might not put their produced lithium back into the interstellar medium rapidly enough. An alternative supernova source for ^7Li is the ν-process of Woosley, et. al. (1990). However, there is some concern that the ν-process may tend to overproduce ^{11}B as well as rare odd-odd nuclei such as ^{180}Ta if it yields significant ^7Li.

A related question to all of this is that of the ^{11}B abundance. BBN models do not make ^{11}B . It is generally assumed that ^{10}B and ^6Li are made by Galactic cosmic ray spallation of heavier nuclei (Reeves, Fowler, and Hoyle (1970)). However, cosmic ray spallation produces (Walker, Matthews, and Viola (1985)) ^7Li and ^6Li in the ratio $^7Li/^6Li \sim 2$ whereas solar system observations (Cameron, 1982) yield $^7Li/^6Li \sim 12$ in agreement with the lower bound of $^7Li/^6Li \gtrsim 10$ in F and G stars determined by Anderson, Gustafsson and Lambert (1984); for the interstellar medium towards Zeta Ophiuchus, Ferlet and Dennefeld (1984) find $^7Li/^6Li \sim 38$ ($\gtrsim 25$). Spallation also produces ^{11}B in an isotope ratio $^{11}B/^{10}B \sim 2.5$ whereas the observed (Cameron 1982) boron isotope ratio is $^{11}B/^{10}B \sim 4$. Thus, if spallation produces ^6Li and ^{10}B (for which there are no other proposed mechanisms, since both ^6Li and ^{10}B seem too fragile for stellar production), it is unlikely that spallation can account for all ^7Li and ^{11}B production as well. Since the limiting reaction for ^7Be production in Cameron-Fowler schemes is $^7Be\,(\alpha,\gamma)^{11}C \rightarrow e^- + ^{11}B$ we might suspect that the supplemental ^7Li and ^{11}B sources could be identical.

In 1973, it was proposed by Colgate (1973) and Hoyle and Fowler (1973) that deuterium and other light elements might be created if a strong ion shock were produced in the very low density ($\sim 10^{-5} g/cm^3$) region of the hydrogen envelope of a core collapse supernova. Epstein, Arnett, and Schramm (1976) noted that

in this case, ^7Li and ^{11}B were particularly easy to make in the ion shock process. Since lithium and boron are rare, this limited the process, if it occurred at all, to the production of only ^7Li and ^{11}B and ruled out D production in this process. Weaver (1976) showed that for envelope shock models of up to very high energies:

$$\text{for } E_{shock} < 100MeV/nucleon \equiv m_H v_{shock}^2/2 \rightarrow v_{shock} = 1.4 \times 10^{10} cm/s, \quad (1)$$

(where m_H is the mass of a hydrogen atom) the shocked gas remains essentially in radiative equilibrium and thus such shocks are mediated almost entirely by radiation (*i.e.*there was no significant ion shock). This implied that in the relatively diffuse medium of a red giant envelope, the shock-induced temperature jump was too small by the time the shock reached the base of the surface convection zone, where ^3He could be found to use as a starting material for ^7Be synthesis, to produce significant ^7Li . However, Arnould and Norgaard (1975) showed that for certain generic explosive nucleosynthesis environmental conditions (we will discuss this scenario below), significant ^7Li production could occur. With the explosion of SN1987A, attention turned to the specific dynamics of core collapse in blue giant stars. DSST argued that in these stars, with their more compact envelopes, shock temperatures sufficient for ^7Li and ^{11}B production might occur around the base of the ^3He zone, that is, processing conditions utilized by Arnould and Norgaard might occur (see figure 2). However, they noted the sensitivity of their conclusions to the shock assumptions. They also admitted that the shock physics used in their calculations might be less detailed than necessary for accurate conclusions. In this paper, we have used a state of the art calculation of the envelope shock dynamics to explore the sensitivities of the models. In particular, we note that our current, more detailed treatment of the shock puts more energy into radiation pressure than the model of Dearborn et. al. This results in a lower temperature behind the shock front for a given configuration and thus less light element production. Woosley, et. al. (1990) have not only proposed a different mechanism (*i.e.* neutrino induced reactions) which could produce ^7Li and ^{11}B deeper in the supernova than the zones we consider but also questioned

whether the results of Dearborn et. al. would be confirmed by detailed modeling, since the post neutrino shock wave processing calculations in their models produced significantly smaller light element yields.

In the rest of this paper, we first discuss the models used to create the presupernova stars. We then give a detailed description of each of the components of the simulation of the envelope shock: the underlying Von Neumann-Richtmeyer artificial viscosity hydrodynamics code, our method of treating radiation pressure and transport, the approximations we assumed in modeling the fundamental physics of the gas of the stellar envelope, the "piston" which we used to drive the explosion, and our thermonuclear reaction network. Next, we discuss our methods for checking the reliability of the code. Finally, we present our conclusions about the supernova shock yields of ^7Li and ^{11}B and discuss their significance in the light of the overall picture of Galactic chemical evolution and of other proposed production mechanisms.

The Input Models

Figure 2 shows a schematic of a typical stellar model immediately before it explodes. There is a very dense ($\sim 10^4 g/cm^3$) carbon/oxygen core surrounded by a carbon shell ($\sim 10^3 g/cm^3$), a helium shell ($\sim 100 - 10 g/cm^3$), and an extended hydrogen envelope containing $60 - 65\%$ hydrogen by mass. There is a surface convection zone which mixes the material in the outer envelope down to the region where the H and ^4He mass fractions are approximately equal. This convection brings original ^3He (*i.e.* the ^3He that the star was "born" with plus the primordial ^2H that had burned to ^3He during its lifetime) down to this point. The increased temperature will destroy most of the ^3He present below the base of the convection zone, but a substantial amount ($X \approx 10^{-4}$) of ^3He will be present at this point. As the supernova shock weakens in its passage through the outer envelope, the temperature immediately behind the shock (the region where our proposed synthesis will occur) decreases such that the closer the innermost ^3He containing zone is to the center of the star, the more ^7Li should be produced. We expect that blue progenitor stars, with their more compact outer envelopes, will

produce considerably more ^7Li than red stars. The higher densities in the blue stars which lead to generally higher post-shock temperatures should also favor them as ^7Li production sites. These conjectures are born out by our simulations.

Specifically, the supernova precursor models we used came from the evolution of 15, 25, and 100 solar mass stellar models which started with initial compositions of a H mass fraction of .7, a metallicity $z = 0.02$ (standard Pop I metallicity), and a ^3He mass fraction $X(^3He) = 2.1 \times 10^{-4}$. This ^3He value assumes that all initial deuterium is processed to ^3He during the protostellar collapse phase (Dearborn, Schramm, and Steigman 1985). The models were evolved from the zero age main sequence into the core carbon burning phase, after which no additional nucleosynthesis occurs in the envelope prior to the core collapse. Since we will only be concerned with processing in the outer envelope, the models were not evolved past this point. A more complete description of the stellar evolution code used can be found in the appendix to Dearborn, et. al. (1990).

The radii of red giant models are sensitive to the surface opacities and the mixing length. For this reason, the mixing length is often taken as a free parameter to fit the observed temperature of stars in a cluster. In our red giants (models m150 and m151), we used models with slightly different ages, as well as different mixing lengths (Table 1). While the radius of a star at the end of its lifetime is quite uncertain, we can be guided by comparison of our models with observations. Brown, Tomkin, and Lambert (1983) examined the available observations of Betelgeuse and found it to be a 15 solar mass star with a radius between 4.26 and $4.67 \times 10^{13} cm$. Since it is a variable, the precise radius at the time of its core collapse cannot be pre-determined. Our models m151 and m152 are, however, quite representative of Betelguese. The envelope contains 7.2 solar masses of hydrogen, and 11 solar masses total. The models are convective in the outer 10.5 $M_\odot$, and the ^3He mass fraction is a constant through this region, at approximately 10^{-4}. Below the base of the convection zone, the abundance of ^3He falls discontinuously to its equilibrium value outside the Hydrogen burning shell.

Although our stellar models go through a "blue loop" period during Helium

burning, they all evolve to the red before the core collapse occurs. It is known that the outer hydrogen envelopes of giant stars can alternate between extended (red) and compact (blue) phases regardless of the evolutionary state of their cores, so that they may experience core collapse in either red or blue states. In particular, SN1987A exploded from a blue progenitor. In order to obtain a "blue" envelope structure that is similar to that which SN1987A must have had, we took models at a slightly earlier evolutionary phase, the end of helium burning and the beginning of carbon burning. Our models at this stage were still on a "blue loop" and had not yet returned to the red. Lithium production in such a star requires it to have had a red giant stage with its attendant convection zones, in order to distribute the surviving ^3He to the deeper regions of the outer envelope. Following this, the blue loop causes some additional ^3He depletion in the deeper regions.

In order to cover a wide range of possible input models, we also used a model of a $100M_\odot$ star in two configurations. We used one model with absolutely no mass loss (almost certainly an incorrect model), and one with mass loss included (final pre-explosion weight $58M_\odot$). Since our experience indicated that we could expect much greater ^7Li production in bluer models, and since we wanted to explore whether these extremely massive stars would show substantially different behavior from the lower mass models, we exploded these two models while they were in their "blue loop" state.

Since ^3He is not present below the outer edge of the ^4He zone, this was a convenient point at which to initiate our simulation. The outer envelope, starting at the outer edge of the ^4He zone, was "clipped off" and a "piston" was attached to the innermost zone. The "piston" driver which we used to simulate the behavior of the ejected material coming from the core of the star was modeled by fixing the velocity of the innermost zone to a specific predetermined function of time (see below). For modeling of the piston velocity, it is necessary to describe the outer hydrogen envelope as a set of regions of power law density decrease such that

$$\rho = ar^{-\omega} \tag{2}$$

where ρ is the density, a a constant, r the radius, and ω the powerlaw exponent. We chose regions by inspection from a log-log graph of ρ vs r (see figure 3a). As can be seen, the envelope can be conveniently subdivided into a small number of regions of nearly exact powerlaw behavior. We found omega by a chi-squared linear regression fit for each "hand picked" region. Our linear correlation coefficients ranged between .97 and 1.0, where 1.0 is a "perfect" line. Alternatively, our standard (see, for example, Press, et. al. (1988)) estimated errors in slope (ω) ranged from $0.3 - 5\%$.

The zoning structure used for the stellar evolution code is not very useful for our purposes. The zones are much too thick for the detailed examination of the primary area of interest centered around the base of the surface convection zone, we rezoned the models using the following prescription. All zones of mass $10^{30} - 10^{32}g$ were not changed. Zones of mass $> 10^{32}g$ were cut into an integral number of equal mass zones, such that their masses were as close to $10^{32}g$ as possible. Zones of mass $< 10^{30}g$ were grouped together into a single zone until that zone's mass was $> 10^{30}g$. Since this new zoning was not in strict hydrostatic equilibrium and since it resulted in adjacent zones of up to 50% difference in mass, in higher energy shocks there was some slight ($\lesssim 10\%$) "ringing" of the hydrodynamic variables behind the main shock due to small shocks traveling between the real shock front and the beginning of the rezoned region.

The Simulation

HYDRODYNAMICS

The hydrodynamic code we used was a modified version of the SIMPLE code (Larsen 1989). This code is a one-dimensional (spherically symmetric, cylindrically symmetric, or slab geometries can be selected) Lagrangian mesh model. The SIMPLE code treats the gas in which the shock takes place as three separate fluids (electrons, ions and radiation) and links them together with simplified models of the relevant physics. We ran the simulations in "full ionization" mode,

i.e. assuming that the nuclei were completely ionized at all times (essentially exact, since the lowest temperatures we dealt with were in excess of 10^6 $^\circ K$). Since we did not run with full radiation transport (see below), this ionization assumption did not affect the *opacity* of the stellar material but only affected the hydrodynamics and heat diffusion parts of the code. The electrons, the ions, and the radiation were thus considered as three separate fluids, loosely coupled. For the electrons and the ions, we assumed a perfect gas equation of state.

Radiation Transport and Pressure

Since the radiation pressure can range from being about equal to the matter pressure in front of the shock to more than 100 times the matter pressure behind the shock, it is important that this be treated properly. SIMPLE normally uses a full flux limited diffusion treatment of the radiation transport in the gas. For full diffusive radiation transport treatments to run in a reasonable amount of computer time, the zone size should be somewhere close to the actual optical mean free path. In a stellar interior, this mean free path is meters at most. With the large size of our area of interest our single zones were at least $1,000$ km wide, so it was impossible to run simulations with full radiation transport in any available amount of computer time. Fortunately, this was not necessary. As we mentioned above, Weaver (1976) has shown that under the conditions present in supernova envelope shocks, the fluids should remain essentially in radiative equilibrium. Thus, we could mimic full radiation transport by assuming that the three fluids always maintained the same temperature and we modified the code to enforce this condition. To insure the optically thick approximation, we also set the opacity to a high value ($10^5 cm^{-1}$); a realistic, appropriate, calculated opacity would have varied over a large range, but the corresponding optical mean free path would have remained much smaller than our zone size, so we chose the fixed value for efficiency. This high value for the opacity helped to insure that the radiation remained in equilibrium with the other fluids. Our radiation treatment then consisted of an electron-radiation coupling routine, a flux-limited radiation pressure term, and a routine which summed the total energy present and apportioned it between the three fluids such that they all maintained the same

temperature. In order to check further both the equal temperature assumption and the general appropriateness of our overall radiation handling scheme, we ran the complete code on a finely zoned test case with full multi-group radiation transport. (Multi-group refers to the fact that we could break the radiation into frequency ranges which are treated separately by the radiation diffusion routine, to allow for departures from a purely Planckian local thermodynamic equilibrium distribution). For our test runs, the radiation was treated in 50 frequency groups. The zones were $100cm$ thick, approximately one optical Rosseland mean free path. The test was run in slab geometry for convenience. The entire test model was only $2,500cm$ thick. We input a shock with a velocity of $2.2 \times 10^9 cm/s$. Comparisons of the results for full transport and our approximation, at $6 \times 10^{-7} s$ and $10^{-6} s$, are shown in figures 4 and 5 and the temperatures can be seen to agree to a very high degree ($\lesssim 3\%$). A detail of the three fluid temperatures near the shock front in the full radiation transport case is shown in figure 6. It can be seen that shock structure in the form of a *small* ion temperature spike only appears on a scale of $\sim 10 - 20\ cm$ ($\sim 1 - 2$ zones immediately behind the shock front), very much smaller (by a factor of 10^{-7}) than our usual zone size. Further, the difference between the radiation and ion temperatures is only $\sim 0.6\%$. Thus, we see that our equal temperature approximation is validated as predicted by Weaver (1976).

Assumed Mechanisms of Importance

The shock was mediated by an artificial quadratic viscosity term in the ion hydrodynamics in the form of an added pressure P_Q:

$$P_Q = \begin{cases} 2.0\rho(\Delta x)^2(\frac{\Delta u}{\Delta x})^2, & \text{if zone is in compression, } dV/dt < 0 \\ 0 & \text{otherwise} \end{cases} \qquad (3)$$

where ρ is the matter density, Δx is the zone size, V is the zone volume, and Δu is the difference in velocity accross the zone. The multiplier of 2 is chosen by tradition. Test runs with other quadratic viscosity multipliers showed little variation in results apart from a slight rounding and smoothing effect at the leading shock

edge (see table 2). Full discussions of the Von Neumann-Richtmeyer artificial viscosity prescription in numerical hydrodynamics can be found in Larsen (1989) or Mihalas and Mihalas (1984) (among others). The real physical mechanism of shock mediation in the regime of interest is radiation pressure, but ion viscosity was easier to implement in our code. The forced equilibrium described above makes our method equivalent to radiative mediation (see also the discussion of analytic Hugoniot relations below for confirmation). Since our shock velocities are $\lesssim 4 \times 10^9 cm/s \approx 20 MeV/nucleon$ we are justified in using a non-relativistic ($\lesssim .1 - .2c$) assumption with respect to the overall velocities involved. More importantly, our post shock temperatures remain below $100keV$, so that our non-relativistic ideal gas equation of state remains valid. Another important approximation is that we have assumed a lack of significant spontaneous electron positron pair production. Weaver (1976) has derived a criterion for whether pair creation processes are important (*i.e.* when the number density of pairs equals the number density of ions):

$$E_0 \gtrsim .95 \Phi^{-5/2} e^{\Phi} \tag{4}$$

$$\Phi \equiv \frac{m_e c^2}{k T_1} = \frac{5.94 \times 10^9}{T_1} \tag{5}$$

where m_e is the electron mass, T_1 is the immediate post shock temperature in Kelvin, and E_0 is the shock strength in $MeV/nucleon$. From this we can calculate that, since our shocks remain $< 20 MeV/nucleon$, our post shock temperatures must remain below $62keV$ (which they do) if we are to be correct in neglecting pairs.

We also included the effects of gravity in our simulations, but these turned out to have a negligible effect on the hydrodynamics and the nucleosynthetic yields.

MODELING THE "PISTON"

To avoid the still unresolved question of the precise mechanism of shock production in core collapse supernovae, we placed a "piston" at the base of our envelope model and set it in motion with a test velocity. Its subsequent evolution was determined by the analytic models of Sedov (1959) for the propagation of a strong shock in a $\gamma = 4/3$ gas (*i.e.* pure radiation) with a power law density profile. We changed power law exponents whenever the shock front entered a new region (figure 3) since the overall shape of the shock velocity distribution as it propagates will approach the shape characteristic of whatever the current power law is (Chevalier 1976). Thus, the shock front first accelerates as it comes down the steep ($\omega > 3$) gradient of the edge of the helium zone, but then quickly (within $\sim 10sec$) becomes a decelerating shock as it settles into the $\omega \approx 2 - 2.5$ region, which makes up the main body of the hydrogen envelope (and covers all of the narrow region of interest) (figures 2, 3, 7). We could also tell by inspection if there was an error in the velocity source since, after an initial energy transfer phase ($\sim 10 - 30\ sec$), the innermost zone ("piston") should follow smoothly along behind the zones in front of it neither crowding them nor lagging them significantly. We could also observe any energy input or removed by an improper source function, after the initial energy transfer, by following the overall energy budget edits produced by the code (see below).

In order to create a piston which will properly "follow along behind" the post shock material, we used the Sedov similarity solutions for a propagating shock in a material with power law density falloff. As described above, we can approximate the density gradient in various regions of the star with a power law (see figure 3). The Sedov solutions then provide us with analytic formulas for the position of the shock front and a parametric set of equations from which we can derive the position of any zone behind the front at a particular time after the shock passes it. In practice, we characterize the strength of the shock by a parameter $\xi \propto E_0/(5-\omega)$ where E_0 is the total energy of a spherical shock blast in an infinite, perfect powerlaw density distribution of an ideal gas (initially unknown since the starting *velocity* is our independent variable), and ω is the

density exponent as given in equation (2):

$$\xi \equiv r_0 t_0^{\frac{2}{\omega-5}}. \tag{6}$$

Here t_0 is the time it would have taken in a power law medium for the shock wave to travel from the blast center to the piston zone radius, r_0.

$$t_0 = \frac{4r_0}{v_0(\omega-5)(\gamma+1)}, \tag{7}$$

where γ is the perfect gas specific heat ratio. Since we start our simulation at $t_{sim} = 0$, the time, t in the subsequent Sedov equations is:

$$t \equiv t_{sim} + t_0 \tag{8}$$

If, in addition, we let r_2 be the radial position of the shock front, v_2 be the (lab frame) velocity of the gas immediately behind the shock, and v be the velocity of the piston, then the Sedov equations for t and v in terms of the parameter V are:

$$r_2 = r_0 \; g(\gamma, \omega, V) \tag{9}$$

$$t = \frac{r_2^{\frac{5-\omega}{2}}}{\xi} \tag{10}$$

$$v_2 = \frac{2r_2}{(5-\omega)t} \tag{11}$$

$$v = \frac{1}{4} v_2 (5-\omega)(\gamma+1) V f(\gamma, \omega, V) \tag{12}$$

where

$$g(\gamma,\omega,V) = \left[\frac{(5-\omega)(\gamma+1)}{4}V\right]^{2/(5-\omega)} \left[\frac{\gamma+1}{\gamma-1}\left(\frac{\gamma(5-\omega)}{2}V-1\right)\right]^{-\alpha_6}$$

$$\left[\frac{(5-\omega)(\gamma+1)}{7-\gamma-(\gamma+1)\omega}\left(1-\frac{3\gamma-1}{2}V\right)\right]^{-\alpha_7} \left[\frac{\gamma+1}{\gamma-1}\left(1-\frac{(5-\omega)}{2}V\right)\right]^{\alpha_6+\alpha_7-[2/(5-\omega)]} \tag{13}$$

$$f(\gamma,\omega,V) = \left[\frac{(5-\omega)(\gamma+1)}{4}V\right]^{-2/(5-\omega)} \left[\frac{\gamma+1}{\gamma-1}\left(\frac{\gamma(5-\omega)}{2}V-1\right)\right]^{-\alpha_2}$$

$$\left[\frac{(5-\omega)(\gamma+1)}{7-\gamma-(\gamma+1)\omega}\left(1-\frac{3\gamma-1}{2}V\right)\right]^{-\alpha_1} \tag{14}$$

$$\alpha_1 = \frac{(5-\omega)\gamma}{3\gamma-1}\left[\frac{2(6-3\gamma-\omega)}{\gamma(5-\omega)^2}-\alpha_2\right] \qquad \alpha_2 = \frac{\gamma-1}{(\omega-1)\gamma-1} \tag{15}$$

$$\alpha_6 = \frac{\gamma}{(2\gamma+1-\gamma\omega)} \qquad \alpha_7 = \frac{\alpha_1(3\gamma-1)}{6-3\gamma-\omega} \tag{16}$$

Thus, we can now substitute V's into these equations and get out pairs of (t_{sim}, v) which we feed in as a rigid velocity source for the innermost zone of our mesh. We also keep track of the value of r_2 and, when r_2 (*i.e.* the position of the shock front) enters a new density powerlaw region, we take the t, v, and r at that point and use them as t_0, v_0, and r_0 for a new calculation with the ω appropriate for that region. In these calculations, we have used $\gamma = 4/3$ since the "radiation gas" is the actual primary mediator of the shock and the Sedov solutions are a "one-fluid" model and should thus be solved for the dominant "fluid". In our case this is the photon gas (see Chevalier 1976). We should here note that model o58 has an odd quirk in its structure with *two* power law regions with ω significantly greater than 5. In the other cases, such regions were small in terms of the time the shock spent in them and came at the start of the simulation only; thus,

approximating ω with 4.9 posed no major difficulty. In this case, however, the presence of such large regions of high ω caused the code to be very unstable to "overdriving" errors, so we attempted to get a reasonable piston velocity profile by "turning off" the piston (*i.e.*setting the velocity to a value of about 1/10 of the starting velocity) after 50 seconds. The shock continued to propagate nicely, but with some "pinning down" of the shock tails as in the linear piston case (Figure 12). Since the post-shock temperature was still well below the critical temperature of $\sim 10keV$ this should not change the final yields by a great deal.

THE REACTION NETWORK

The network of reactions we used is shown in table 3. The thermonuclear reaction rate values were taken from Coughlan and Fowler (1988). We chose this particular set of reactions by examining their tables of rate versus temperature. We began with the fundamental reaction of interest, $^3He(\alpha,\gamma)^7Be$, and then followed each possible reaction with the ambient nuclides (α, ^3He , H) until each possible branch hit a "wall", *i.e.* a reaction which would not occur below $\sim 100keV$. We then cast this network into an implicitly differenced routine which would evolve the network with time. We found that at our temperatures of interest, the network was stable up to timesteps of $0.5s$. To justify the completeness of picking just these reactions, we used our implicitly differenced mesh to recompute the generic explosion models of Arnould and Norgaard (1975). They used a complete light element network containing 42 nuclei linked by 178 reactions and β decays. For a model temperature vs time profile they assumed Arnett's (1969) generic explosive nucleosynthesis formulation, in which one assumes that an ideal gas is instantaneously compressed to an initial density, ρ_i and temperature T_i. The gas then exands adiabatically so that:

$$\rho = \rho_i e^{-t/\tau_{ex}} \tag{17}$$

$$T = T_i e^{-t/3\tau_{ex}} \tag{18}$$

where τ_{ex} is a characteristic gravitational free expansion time scale:

$$\tau_{ex} \equiv \chi 446 \rho_0^{-1/2} \tag{19}$$

and χ is considered a free parameter. Figure 8 shows the results of running our nucleosynthesis network using the same conditions as Arnould and Norgaard. A comparison with their figure 4 reveals only small differences, with the exception of the final ^3He abundance which is a factor of ten lower. This is due to the higher $^3He\ (\alpha,\gamma)^7Be$ rate used in our network, which leads to a more rapid depletion of ^3He in our case and consequently a lower final abundance. This rate was recently revised as the result of new experiments (see Coughlan and Fowler (1988) and Kawano, Schramm, and Steigman (1988) and references therein). We also compared our numerical mesh (without the nonlinear $^3He+^3He$ term) to an analytical solution of the differential equations (solved for a fixed temperature) obtained by the Laplace transform method. We used the same starting composition of nuclides as in the Arnould and Norgaard simulations. Figure 9 shows the two models and, except for the slight irregularity in the destruction curve of ^{11}B at times of $\sim 10^{-5}$ to $10^{-2}s$, they are identical. As a point of interest, inclusion of the $^3He+^3He$ reaction results in a slightly faster destruction of the ^3He starting material and corresponding lowering of the yields of all of the other products (see figure 10).

A close examination of the results of these simulation will disclose the overall path of Cameron-Fowler lithium synthesis. Figure 10 illustrates the reactions involved. The basic paths are:

$$^3He + ^4He \rightarrow ^7Be + \gamma \tag{20}$$

$$^7Be + ^4He \rightarrow ^{11}C + \gamma \tag{21}$$

The ^7Be and ^{11}C will become ^7Li and ^{11}B by electron capture and positron emission, respectively, as the ejected material cools. Any initial ^{11}B is quickly destroyed by protons. Interestingly, this whole scheme would be phenomenally unproductive if it weren't for the photodisintegrations. One would expect that

proton destruction of both ^{7}Be and ^{11}C into ^{8}B and ^{12}N should be disastrous for this mechanism, since both ^{8}B and ^{12}N very quickly β decay into 2 α's and ^{12}C respectively. However, at temperatures above 1.2×10^{8} for ^{8}B and 4.8×10^{8} for ^{12}N the photodisintegration of these elements back into ^{7}Be and ^{11}C takes place at a faster rate than beta decay. This behavior is evident in figure 8, where first the ^{12}N and then the ^{8}B show fairly sharp "bumps" as the temperature falls off. This is due to a rapid rise in their abundances as the photodisintegration becomes negligible followed by a decrease in abundance as the production reactions for ^{8}B and ^{12}N also cut out with falling temperature, thus allowing them to beta decay away. This same basic pattern of events will characterize any Cameron-Fowler type light element synthesis environment: that is, any one characterized by a sharp, large temperature increase followed by rapid cooling.

Quality Control

After glancing over the Sedov equations for a propagating shock, the first quality control question the reader may be tempted to ask is just how sensitive the light element production is to the piston velocity curve. To test this qualitatively, we ran three simulations of approximately the same final energy (as determined by the energy audit of the simulation code) but with radically different piston velocity curves (shown in figure 11). The "correct" curve was formed by the method described above. The "bad" curve was formed by the above method as well, but a much higher starting velocity was combined with the wrong density power law exponents, ω's (we leave it to the reader's imagination to discern the circumstances of this simulation's generation). The "linear" piston function was produced merely by drawing a line between two of the points of the correct curve. Velocity and temperature profiles for the three pistons are shown in figures 12 and 13, and except for the "pinning down" of the piston velocity in the linear case resulting from "overslowing" the piston (an opposite effect occurs if the gas is "overdriven" by a piston moving too fast: velocity and temperature "tails" develop) , there is not a great deal of difference between them. As can be seen from table 4, the ^{7}Li yields are similar (within 34%) and

even the amount of kinetic energy error (see below) is similar. The difference between the ^{11}B yield of the "bad" piston and the other two is a result of the very high initial velocity, which causes a relatively large build up of ^{11}B in the zones immediately adjacent to the piston zone because of the lack of hydrogen, *i.e.* destructive protons, in that region. This production site is not very significant if there is even reasonably efficient production of ^{11}B in the same zones as the ^{7}Li production, since ^{3}He is already being turned into ^{7}Li and ^{11}B at 100% efficiency in this region. Thus, more favorable shocks can increase ^{11}B production farther out, but the production at the edge of the ^{4}He zone remains fixed. For example, in the case where we ran a trial version of the code with zero radiation pressure resulting in very high post-shock temperatures, the contribution of the inner zones to the total ^{11}B production was small (less than 5%).

In terms of overall quality control, we used two methods to determine whether the shock structure was accurately modeled. First, we compared our shock structures at given instants to the the general effective photon shock model Hugoniot relations of Weaver (1976), which describe the "jump" in the values of of the hydrodynamic variables across a shock front of arbitrary strength. In Weaver's non-dimensional form these are:

$$\chi_q \eta_f \tau_f^4 + 2\tau_f = \eta_f(-\eta_f + \epsilon_o + 1) \tag{22}$$

$$3\chi_q \eta_f \tau_f^4 + \tau_f(\alpha_e + 3/2) = 1/2(1-\eta_f)(1-\eta_f+2\epsilon_o) + \alpha_o \epsilon_o \tag{23}$$

where:

$$\alpha_o = \frac{3(1+\chi_o)}{2+\chi_o}, \qquad \chi_o = \frac{18.27 T_o^3}{n_o}, \qquad \alpha_e = 3/2\left(\frac{5}{\frac{2.373\times10^{18}}{T_f+5}+1}\right) \tag{24}$$

$$\epsilon_o = \frac{(\chi_o+2)kT_o}{mv_o^2}, \qquad \chi_q = \frac{6.95\times10^{48} m^3 v_o^6}{n_o} \tag{25}$$

$$\tau_f = \frac{kT_f}{mv_o^2}, \qquad \eta_f = \frac{v_{gas}}{v_o}. \tag{26}$$

In terms of our parameters these can be rewritten in the form of the continuity equation

$$\kappa \equiv 1 - \frac{u_{gas}}{u_0} = \frac{\rho_0}{\rho_1}, \tag{27}$$

the momentum conservation equation

$$2\kappa R\rho_0 T_1 + \frac{4\sigma}{3c}T_1^4 = \rho_0 u_0^2(1 - 1/\kappa) + \frac{4\sigma}{3c}T_0^4 + 2R\rho_0 T_0, \tag{28}$$

and the energy conservation equation

$$(2\alpha_e + 3)\kappa R\rho_0 T_1 + 6\frac{4\sigma}{3c}T_1^4 = \rho_0 u_0^2 \kappa(1 - 1/\kappa)^2 + 2\frac{4\sigma}{3c}(4\kappa - 1){T_0}^4 + 2\rho_0 R T_0(5\kappa - 2). \tag{29}$$

$$\alpha_e \equiv 3/2(\frac{5}{\frac{2.373\times10^{18}}{T_f} + 5} + 1) \tag{30}$$

In these expressions, T_0 and ρ_0 and T_1 and ρ_1 are the temperature and density immediately in front of and behind the shock, respectively, u_0 is the speed of the shock front relative to the unshocked gas, and u_{gas} is the (lab frame) velocity of the gas behind the shock. All quantities are in cgs units and temperature is in °K . Readers familiar with the totally opaque gas, strongly radiative shock approximation (see *e.g.* Mihalas and Mihalas (1984)) will note that this energy equation is different. This is due to the inclusion of terms accounting for the energy flux across the shock front. Thus, while a completely ion mediated shock (*i.e.* no radiation pressure) will produce spuriously high temperatures behind the shock, what one might naively consider a fully radiating shock creates post-shock temperatures which are a factor of ten or so too small. Table 5 shows the comparison of our simulation and the Hugoniot relations for a wide variety of conditions

which span those encountered in our models. The error is generally between 5 and 10 % with a few larger errors appearing non-systematically. The greatest source of error here (easily up to 10% in any case) is due to the impossibility of actually locating the shock front in an artificial viscosity code. To measure the speed of the shock front (our shock strength defining parameter), we noted every few cycles of the code which zone was controlling the time step. This zone corresponded to the one with the greatest compression and so "contained" the shock front at that time. By dividing the original width of the zone by the time the shock spent in it, we obtained an estimate of the speed of the shock. Because of the finite size of these zones (each was 100 cm initially), the finite size of the timestep, and the spreading of the front over more than one zone in the weak shock cases, this could lead to significant "error" which does not reflect an inaccuracy of the actual hydrodynamics of the code. The other source of error was closely related. Since the zones behind the shock rang (see above) and because the shock is spread over a small number of zones it was often difficult to determine which zone to use for the actual peak post-shock velocity and temperature. In some cases where we checked, there was as much as 10 % difference between adjacent zones behind the shock. Considering these uncertainties, the results in table 5 indicate good agreement between our code and the analytic predictions of the Hugoniot relations.

The second check was to track the overall energy flow between the thermal energies of the three fluids (electrons, ions, and radiation) and the kinetic energy of the shocked material. By comparing the total kinetic energy created by the source plus the initial thermal energy of the mesh with the total energy present in the mesh at any time, we could tell if there was any significant unaccountable loss or gain in energy. The generally accepted rule for artificial viscosity codes is that overall energy error should not exceed $\sim 10 - 20\%$. By far the largest errors occur in kinetic energy, while the internal energies of the electrons and ions always remain much smaller than the kinetic energy error. A large part of this "error" is created by the way the hydrodynamic equations are transformed into difference equations. For stability reasons, the algorithm is structured so that the position of a zone is correct at the end of the time step, but the velocity

is off by approximately one-half of a time step. Thus, when the code calculates the current kinetic energy, it uses the velocity at the previous half time-step. If the velocities are changing rapidly (which is true at the shock front) this can create an "error" which looks like missing kinetic energy. Our errors ranged from $\sim$ 20% to $\sim$ 4% with few exceptions. These were all in the very low energy shocks in the heavy blue stars. This error comes from at least two sources. First, the post shock ringing discussed above is much closer in magnitude to the actual shock size in these very weak shock situations. Further, gravitation (which was added on to the finished code, and thus not included in the energy conservation routines) while having an almost imperceptible effect ($\sim$ 1%) on light element yields, did cause a comparatively large "error" in the kinetic energy of these weak shocks. It should also be noted that these errors build up with time since the error per step remains fairly constant (with some decrease as the shock gets weaker), and are much smaller at the end of nuclear burning around 100 seconds than they are at the very late time of 1,000 seconds reported for most of the simulations. For instance, model m251 with shock energy $3.05 \times 10^{50} ergs$ at 150 seconds has deposited all of its piston energy in the outer envelope (*i.e.*the piston is "coasting") and has finished both ^{11}B and ^{7}Li production, but it has only a 14% kinetic energy error as opposed to 38% at 1,000 seconds.

As a final qualitative check we "kept an eye on" the overall shape of the shock as it evolved to make sure no "tails" or "pinning down" occurred, as in the linear piston case shown in figures 12 and 13 and in the o58 model as discussed above.

Results and Conclusions

Our overall ^{7}Li and ^{11}B yields for a range of energies and precursor masses are shown in figures 14–19and in table 6. Most of the simulations were run for 1,000 simulation seconds at which point the maximum shock temperature was well below the minimum temperature for nuclear processing of 1×10^{7} $^{\circ}K$. The exceptions were the very high energy shocks run on the m251 model and the the very massive models (o58 and o100), which were run only until the shock left the region of interest (*i.e.*the ^{7}Be and ^{11}B abundances stopped evolving)

because of cpu time constraints. The time evolution for a typical shock passing through the region of interest is shown in figure 20. The ^7Li and ^{11}B were produced exclusively in a region centered about the base of the surface convection zone (within the first solar mass worth of material outside the ^4He core shell) where the hydrogen and helium have approximately equal mass fractions (see figures 21 and 22). For purposes of comparison, in other detailed explosion simulations and in observations the total energy deposited by the shock is found to be $1 - 3 \times 10^{51} ergs$. It should be born in mind that the energy we report is deposited in the outer envelope and does not include energy residing in the ejected core. In table 6, we also give the total kinetic energy present at the stopping points for our simulations. We note that at these points in time, the shock is still deep within the star and therefore most of the shock energy still resides in the radiation immediately behind the shock; this implies that the energy of the core ejecta at the end point of the simulation is comparatively small and thus our reported "total energy" is a good number to compare to the measured kinetic energy at light breakthrough in observations. The shock weakens as it progresses outward to times past the end of our simulations, and thus a progressively smaller percentage of its energy resides in radiation; by the time the shock reaches the surface of the star, most of its energy is thus kinetic (Chevalier, 1976).

As expected, the red giant stars (models m151,m152) are much poorer producers of light elements than are the blue giant stars (all of the other models). The exception to this is the massive star model with mass loss which is a very poor ^7Li producer because it lost most of its ^3He as a consequence of mass loss, and thus had a much lower preexplosion ^3He abundance than the other models (see table 1). It is also clear that only at very high shock energies, $\gtrsim 4 \times 10^{51}\ ergs$, in our most favorable models involving large blue giant pre-supernova stars, does this process even reach a Pop I ^7Li abundance overall in its ejecta. For energies ($\sim$ 10 times) higher than observed, the ^7Li mass fraction averaged over the total ejected mass of the star is still only 5×10^{-9}.

Figures 18 and 19 show the total mass of ^7Li and ^{11}B produced as a function of stellar mass for the most productive pre-supernova models (including the unrealistic o100). There is not much variation in production over this wide mass

range. Thus, it seems unlikely that there is a hidden "super-producer" class of stars. We shall discuss below how to recognize such a class of models if they do appear in future research, however.

As derived in DSST, we may compare our yields to the expected iron production of core collapse supernovae. As argued by Arnett, Schramm, and Truran (1989), because the central cores of all Type II supernovae are so similar, we might expect them all to yield comparable quantities of iron to that determined for supernova 1987A, or $\sim 0.07 M_\odot$ of iron. Type I supernovae can also account for a significant fraction of the galactic iron. Thus, to be a useful source of ^7Li and ^{11}B, the ratios Li/Fe and B/Fe in the ejecta must be greater than or comparable to present values in the Galaxy. DSST then use these numbers to obtain the result that, to within factors of a few, a "critical" yield of lithium in a supernova is

$$log\ M(Li) = -6.3 \pm 0.1 \quad M(Li) \gtrsim 4 \times 10^{-7}\ M_\odot. \tag{31}$$

Similarly, for boron they find,

$$log\ M(B) = -6.5 \pm 0.1, \quad M(B) \gtrsim 3 \times 10^{-7}\ M_\odot. \tag{32}$$

However, the lithium vs. iron measurements also indicate that over a range of iron abundance (mass fraction) (Fe/H) from 10^{-4} to $10^{-1.5}$ times solar, the lithium abundance does not increase by more than a factor of 2 (*i.e.*an increase of $\sim 10^{-10}$ in (Li/H)). This implies that the average lithium output ratio from any Type II supernova process must obey

$$(\frac{Li}{Fe} \text{ at } \sim 10^9 yrs) \lesssim \frac{10^{-10}}{10^{-1.5}}(\frac{Li}{Fe} \text{ now}) \quad \approx 10^{0.5} 10^{-6.35} \approx 10^{-5.15}. \tag{32}$$

If we further assume that these supernovae produce $\lesssim .1 M_\odot$ of iron, we obtain

$$M(Li) \lesssim 10^{-5.15} 10^{-1} = 7 \times 10^{-7} M_\odot. \tag{32}$$

Even if we allow for the very approximate nature of the assumptions in these calculations, they indicate that effective supernova production is rather tightly

constrained to a range of about 10^{-7} to $10^{-6} M_{\odot}$ of ^{7}Li per event *averaged over all masses*. This constrained range argues for a slightly "slower" production site such as high mass AGB red giants (see below).

As can be seen in our models, pushed as far as we think reasonable (and about as far as we can trust our code), ^{7}Li yields are still a factor of 80 below this "break even" point and the ^{11}B yield is orders of magnitude too low.

It, thus, seems unlikely that the envelope shock mechanism can independently account for the evolution of ^{7}Li abundances from Pop II to Pop I values. It is important, however, to try to ascertain how firm this conclusion is. In terms of model sensitivity, we have two questions to answer. First, given a potential production site (*i.e.*gas containing ^{3}He), what temperatures and densities are most likely to produce significant amounts of ^{7}Li and ^{11}B ? Arnould and Norgaard (1975) have investigated this in detail, so we can use their results as a guide to determine when more detailed modeling might discover a meaningful production site. Second, since their results require the input parameters ρ_i and T_i (equations (17)- (19)) we must ask what explosive situation will produce this necessary density and temperature. In terms of our envelope shock model, we can use Weaver's (1976) Hugoniot relations for hydrogen envelope conditions to tell us what input shock conditions will produce significant ^{7}Li . Figure 23 details the range of interest for our type of scenario. Post-shock conditions do not depend strongly on pre-shock temperature. We chose 6 keV as a reasonable value for all of the possibilities, since at temperatures much above this no ^{3}He would survive anyway on *stellar* timescales. Then we fed in a range of shock velocities and starting densities. The different symbol types in figure 23 represent different shock speeds. Each point in figure 23 represents an increment of $1 gm/cm^3$ over its neighbor of the same symbol type. The area to the upper right of the line, 'limit', represents Arnould and Norgaard's region of efficient ^{7}Li production for their most productive model. The greatest sensitivity (in terms of conditions that might really be met in stars) is to density variations. At $10,000$ km/s, a maximum reasonable shock speed value in current models, the threshold for significant ^{7}Li production occurs around $\rho = 7$ gm/cm^3. This condition is definitely not met in any current envelope models that we know of. We conclude,

then, that any likely site for shock-induced production of ^7Li would require the presence of ^3He with a mass fraction of $\gtrsim 10^{-7}$ and either a preshock density of $\gtrsim 7\ g/cm^3$ or a shock strength $\gtrsim 20,000\ km/s \sim 1.8\ MeV/nucleon$.

In a subsequent paper (Brown 1990), other non-cosmological sources for ^7Li will be investigated in detail. It may nevertheless be useful to mention briefly the two alternative non-supernovae mechanisms for galactic ^7Li nucleosynthesis which are considered to be promising candidates: those involving classical novae and red giant stars.

Classical novae can produce ^7Li . The critical question is whether they can form sufficient quantities to perhaps make an important contribution to the abundance of ^7Li in the Galaxy. The mode of ^7Li production here is similar that in red giants: ^7Be is carried outward by convection to cooler regions of the envelope on a sufficiently rapid timescale to ensure that it will not be destroyed via $^7Be\ (p,\gamma)^8B$. The total mass of ^7Li ejected is a sensitive function of the conditions achieved in the outburst, particularly the convective history of the ejected matter, and may thus be expected to vary somewhat from event to event. The main problem is the fact that the ^7Li overabundance factors are less than those of other nucleosynthesis products. The hydrodynamic models of Starrfield, et. al. (1988) predict average enrichment factors for the rare isotopes ^{13}C and ^{15}N which are approximately 10 times that of ^7Li . If these relative production ratios are correct, and are representative of classical nova systems, it must follow that novae can account at best for only 10 % of the ^7Li in the Galaxy – when one assumes that ^{13}C and ^{15}N have their origin *entirely* in nova explosions.

The observation of high ^7Li concentrations in luminous red giant stars (Smith and Lambert, 1989) suggests that these may also play an important role in the production of ^7Li in the Galaxy. The difficulty here is to obtain a realistic theoretical estimate on the basis of our current imperfect knowledge of the evolution of the surface compositions of asymptotic giant branch stars. The possibility that red giants may be significant contributors can, however, be demonstrated in a model independent manner. Following the discussion of Scalo (1975), we assume that lithium-rich red giants constitute a fraction 1/100 of the "peculiar"

red giants and that these peculiar giants, in turn, represent a fraction 1/100 of all red giants. Since red giants represent approximately 1/10th of all stars, we then estimate that there are of order 10^{10} red giants. The bright, luminous red giants that show enhanced lithium concentrations are estimated to be losing mass at rates approaching 10^{-7} solar masses per year; such stars also show lithium enrichments of a factor of order 10 to 30 relative to solar system matter. If we take these factors together, we arrive at the following rate of production of lithium in the Galaxy:

$$\frac{1}{100}\ \frac{1}{100}\ 10^{10}\ 10^{-7}\ 10^{-8} = 10^{-9} M_{\odot}/yr \tag{33}$$

If we now assume that this continues over 10^{10} years of galactic evolution and contaminates approximately 10^{10} solar masses of gas in the ISM, we see that red giants can roughly account for the observed ^{7}Li abundance of 10^{-9} by mass. It is clear that a detailed calculation is required that takes properly into account the nucleosynthesis conditions that are believed to obtain in red giants. However, the above argument indicates that we must at least be aware of the possibility that red giants can synthesize lithium. An additional factor to be considered is the fact that they must be able to do this on a relatively rapid timescale, early in galactic history.

In conclusion, Steigman (1990) has done some analytic calculations of lithium evolution in the instantaneous recycling approximation and the preliminary conclusions seem to be that if the lithium "tracks" the iron abundance, it fits the observed data better than if it tracks the oxygen abundance. This would seem to imply that high mass rather than intermediate mass stars are the most likely sites for lithium production. If this is born out by more detailed models, it could point to the need for an effective mechanism of ^{7}Li production in supernovae if the Population II lithium abundance is primordial.

ACKNOWLEDGEMENTS

This work presented as a thesis, by Lawrence E. Brown, to the Department of Physics, The University of Chicago, in partial fulfillment of the requirements for the Ph.D. degree. This work was supported by the DOE and NASA at the University of Chicago and Fermilab (Grant: NAGW-1340), and by the DOE at Lawrence Livermore National Laboratories. We would like to thank James Truran and Gary Steigman for copius help and suggestions. We would also like to thank Dieter Hartmann and Wick Haxton for useful suggestions and discussions.

REFERENCES

Anderson, J., Gustafsson, B., and Lambert, D.L., 1984, *Astron. Astrophys.*, **46**, 2363.

Applegate, J., Hogan, C., and Scherrer, R., 1987, *Phys Rev. D.*, **35**, 1151.

Arnett, W.D., Schramm, D., and Truran, J., 1989, *Ap. J. (Lett)*, **339**, L25.

Arnett, W.D., 1969, *Ap. J.*, **157**, 136.

Arnould, M., and Norgaard, H., 1975, *Astron. Astrophys.*, **42**, 55.

Boesgaard, A.M., to appear in 1990, *Proceedings of the Sixth Cambridge Workshop on Cool Stars, Stellar Systems, and the Sun.*

Brown, J., Tomkin, J., and Lambert, D., 1985 *Ap. J.*, **265**, L93.

Brown, L. E., 1990, in preparation.

Cameron, A., 1982, in *Essays on Nuclear Astrophysics*, ed. C. Barnes, C. Clayton and D. Schramm, (Cambridge: Cambridge University Press).

Cameron, A., and Fowler, W., 1971, *Ap. J.*, **167**, 111.

Chevalier, R., 1976, *Ap. J.*, **207**, 872.

Colgate, S.A., 1973, *Ap.J.(Letters)*, **181**, L53.

Coughlan, G., and Fowler, W. A., 1988, *Atomic and Nuclear Data Tables*, **40**, 283.

D'Antona, F., and Mazzitelli, I., 1984, *Astron. Astrophys.*, **138**, 431.

Dearborn, D., Raffelt, G., Salati, P., Silk, J., and Bouquet, A., 1990, Livermore preprint UCRL-102235.

Dearborn, D., Schramm, D., Steigman, G., and Truran, J., 1989, *Ap. J.*, **347**, 455.

Dearborn, D., Schramm, D., and Steigman, G., 1985, *Ap. J.*, **302**, 35.

Dimopoulus, S., et. al., 1988, *Ap. J.*, **330**, 545.

Epstein, R., Arnett, D., and Schramm, D., 1976, *Ap. J. (Supp)*, **31** 111.

Ferlet, R., and Dennefeld, M., 1984, *Astron. Astrophys*, **138**, 303.

Hobbs, L., and Pilachowski, C., 1988, *Ap. J.*, **334** 734.

Hoyle, F., and Fowler, W., 1973, *Nature*, **241**, 384.

Kawano, L., Schramm, D., and Steigman, G., 1988, *Ap. J. (Lett)*, **327**, 750.

Larsen, J., *SIMPLE: a Hydrodynamics Code for Inertial Fusion Studies*, manual, (Boulder, Colorado: Cascade Applied Sciences), 1989.

Mihalas, D., and Mihalas, B., 1984, *Foundations of Radiation Hydrodynamics*, (Oxford: Oxford University Press).

Press, W. H., Flannery, B. P., Teukolsky, S. A., Vetterling, W. T., 1988, *Numerical Recipes*, (New York: Cambridge University Press).

Reeves, H., Fowler, W., and Hoyle, F., 1970, *Nature*, **226**, 727.

Sedov, V.I., 1959, *Similarity and Dimensional Methods in Mechanics*, (New York: Academic Press).

Scalo, J., 1976, *Ap. J.*, **206**, 795.

Smith, V., and Lambert, D., 1989, *Ap. J. Lett.*, **345**, L75.

Spite, F., and Spite, M., 1982, *Astron. Astrophys.*, **115**, 357.

Starrfield, S., Truran, J., Sparks, W., and Arnould, M., 1988, *Ap. J.*, **222** 600.

Steigman, G., 1990, private communication.

Walker, T., Matthews, G., and Viola, V., 1985, *Ap. J.* , **299**, 745.

Weaver, T. A., 1976, *Ap. J. (Supp)*, **32**, 233.

Woosley, S., Hartmann, D., Hoffman, A., and Haxton, W., 1990, submitted to *Ap. J.*.

TABLE CAPTIONS

1. Model parameters include total mass, envelope mass, hydrogen in envelope, final convection zone ^3He abundance, and the mixing length used in stellar evolution.

2. Results and yields for different quadratic artificial viscosities. These are all model m251 with the same initial input velocity and audited at 200 simulation seconds. There is very little difference between the simulations. Graphs of the hydrodynamic variables show a slight softening (rounding over) of the leading edge of the shock front in the $q = 5$ case.

3. Table of the reactions included in our thermonuclear reaction network.

4. Energetics and final abundances of ^{11}B and ^7Li for the three pistons. Notice that there is scant difference in results except for the higher ^{11}B abundance in the flawed piston model which is discussed in the text.

5. This table shows our systematic check of the numerical code against the supernova envelope shock Hugoniot relations of Weaver (1976). The percent error is rarely more than 10% and only once over 20%. These errors are all attributable to the uncertainty involved in locating the actual shock front and deriving its speed as discussed in the text. The columns give the pre-shock density and temperature (T_0, ρ_0), the velocity of the shock front itself (v_{shock}), and the post shock velocity and temperature (v_1, T_1) calculated analytically with the Hugoniot relations and evolved with the numerical code.

6. This table presents our overall results. The columns give: mass, source energy, kinetic energy, kinetic energy error, simulation seconds run (since errors grow with time), ^7Be yield and ^{11}B yield.

FIGURE CAPTIONS

1. This well-known big bang nucleosynthesis graph shows the primordial abundances of the big bang produced elements vs. the average density (today) of the Universe. The "allowed window" is derived from present limits on the abundances of these elements. Note how the observed Pop II abundance sits right in the dip between the direct ^7Li regime and the ^7Be regime.

2. A schematic cross section of the pre-supernova star. The dotted line marks the lower edge of the surface convection zone which is the main area of lithium production. The drawing is to scale for our model m251 for all but the surface of the star which should be roughly 3 times farther from the center. Radius represents mass enclosed.

3. a) Plot of $log(\rho)$ vs $\log(radius)$ for m251 with the various power law regions marked. We did not compute ω's for more than three regions since our simulations had run their course (*i.e.*the post shock temperature was much too low for nuclear processing) well before the time the shock reached the outer edge of the third region. The slopes and their statistical accuracies are: region I- $\omega = 5.5 \pm .4$, $\rho = .97$; II- $\omega = 2.3 \pm .06$, $\rho = .99$; III- $\omega = 1.713 \pm .006$, $\rho = .9997$. Since the Sedov (1959) solution is only valid for $\omega < 5$ we approximate ω for the first, relatively small, region by $\omega = 4.9$. b) A plot like "a" shown for model o58, note the two areas of high (> 5) ω.

4. Comparison of ion temperature profile with full radiation transport and our approximation using enforced equilibrium of the three fluids at 6×10^{-7} *seconds* and 1×10^{-6} *seconds*.

5. Comparison of velocity profile with full radiation transport and our approximation using enforced equilibrium of the three fluids at $6 \times 10^{-7}s$ and $1 \times 10^{-6}s$.

6. Closeup of the three fluid temperatures vs. radius in the radiation transport test case at $6 \times 10^{-7}s$. Note the essential lack of deviation from complete equilibrium.

7. Velocity vs. time for the piston for model m251, starting velocity $12.6 \times 10^8 cm/s$ (final energy = 1.24×10^{51} $ergs$). Note the rapid initial increase in piston velocity as the shock "rolls down" the gradient at the edge of the ^4He zone, followed by a sharp decline in speed as it begins to sweep up the material in the "flatter" (*i.e.*lower density gradient) region of the star.

8. This log-log plot of abundance vs. time for all of the active nuclides in our network using a $\chi = 1$, $T_0 = 4.5 \times 10^8$ $^\circ K$, $\rho_0 = .911$ generic explosive nucleosynthesis model can be compared with Arnould and Norgaard's (1975) figure 4.

9. Plot of mass fraction vs. time for all of the active (*i.e.*evolving) nuclides in our mesh for the single temperature analytic solutions and the numerical mesh, both computed without the $^3He + ^3He$ reaction. Temperature equals 3×10^8 $^\circ K$. The starting abundances are those chosen by Arnould and Norgaard (1975).

10. Plot of the full numeric solution with the $^3He + ^3He$ reaction for the conditions of figure 9.

11. Velocity vs time for correct ω, flawed ω, and linear pistons. The flawed ω piston starts at velocity $3.78 \times 10^9 cm/s$.

12. Velocity vs radius at 50 second intervals for the three pistons shown in figure 11. Note how the slow speed of the linear piston in the later snapshots "pins down" the tail of the velocity making the linear piston velocity profiles look obviously different from those of the other two pistons.

13. Temperature vs radius at 50 second intervals for the three pistons.

14. The overall output mass fraction (roughly) of ^7Li is given as a function of total input shock energy. The mass fractions are found by dividing the total mass of ^7Li produced in a model (see table 6) by the total starting mass of the star minus $1.4 M_\odot$.

15. This is the same as figure 14 for ^{11}B production.

16. This shows the same as figure 14 but only for model m251 and includes the very high energy shock data.

17. This is the same as figure 16 for ^{11}B .

18. This shows the total mass of ^{7}Li produced as a function of initial star mass for various total shock energies. The models chosen for each mass were those which produced the most ^{7}Li (this includes the naive model o100 with no mass loss rather than the probably more realistic o58).

19. This is the same as figure 18 for ^{11}B .

20. Temperature vs. radius and velocity vs. radius for the main nucleosynthesis part of the simulation for model m251, energy 1.24×10^{51} $ergs$. The curves represent successive "snapshots" at 10, 20, 30, 40 and 50 seconds from start of simulation. At 50 seconds, 99.3% of the final energy of the shock has been transferred from the piston to the mesh, 80% of the final ^{7}Be has been produced, and all of the final ^{11}B has been created.

21. Graph of ^{7}Li mass fraction after shock processing vs mass enclosed (mass shell) for model m251, shock energy = 1.24×10^{51} $ergs$. Note that all of the significant production occurs in a region in mass shell coordinates of $\sim$ $1M_{\odot}$ in width.

22. This is the same as figure 21for ^{11}B . As described in the text, the poor conditions for ^{11}B production in these shocks cause the ^{4}He shell edge production to greatly overshadow the "main production region" which would dominate under more favorable temperature-time profiles. The small feature at the left edge of figure 21 (at $\sim 7\ M_{\odot}$) corresponds to the extremely large feature at the left edge of this figure.

23. This graph plots $\log(\rho_i)$ vs $T_i/10^8$ for different shock strengths. The line, 'limit' represents the edge of the region of significant lithium production in Arnould and Norgaard's (1975) most favorable scenario ($i.e. \chi = 1.0$ in our equation (19)). Each symbol type represents a different shock strength (the number after "v" refers to the speed of the shock front in thousands of km/s). The lower left point in each "v" curve represents a pre-shock density of 1 gm/cm^3 and each point to the right of that represents an increment of 1 gm/cm^3. Thus, the curve v10 crosses the limit line on the seventh dot meaning that a shock with velocity $10,000$ km/s will efficiently

burn any ^3He present into ^7Be if the gas has a density 7 gm/cm^3 before the shock hits. Since the post shock conditions are fairly insensitive to pre-shock temperature, all of the points are calculated for a single pre-shock temperature of 6 keV.

TABLE 1

Model Name	Mass (Solar Masses)	Envelope Mass (Solar Masses)	Hydrogen Fraction of total envelope	X(He3) Maximum[a]	α[b]
m150	15	8.951	.648	1.032E-4	1.4
m151	15	9.647	.625	9.450E-5	1.4
m152	15	9.624	.622	9.441E-5	1.6
m251	25	14.995	.570	8.893E-5	1.4
m252	25	15.009	.555	8.893E-5	1.4
o58	58.6[c]	11.3	.170	6.077E-6	1.6
o100	100	54.7	.435	6.373E-5	1.6

[a] The initial input ^3He abundance, 2.1×10^{-4}, is the same for all models but convection has depleted this abundance. The value in this column is the amount left at the surface of the star (and is approximately constant throughout the convective region of the envelope) immediately before explosion.

[b] α is the ratio of the mixing length to pressure scale height.

[c] This is the final preexplosion mass of the star. It began life as a $100M_\odot$ star but suffered mass loss.

TABLE 2

Viscosity multiplier	source energy ($10^{51}ergs$)	kinetic energy ($10^{51}ergs$)	kinetic energy (% error)	^7Li (solar masses)	^{11}B (solar masses)
0.5	4.11884	1.78566	3.9779	1.58940e-09	9.92745e-16
1.0	4.09850	1.80532	3.0472	1.32150e-09	7.90642e-16
2.0	4.08258	1.83913	2.4725	1.11620e-09	6.29119e-16
3.0	4.06808	1.86078	2.2276	9.87200e-10	5.20774e-16
5.0	4.04182	1.88856	1.9804	8.17190e-10	3.81102e-16

TABLE 3

$$
\begin{array}{lcll}
^3He + ^3He & \longrightarrow & \otimes^a & \\
^3He + \alpha & \longrightarrow & \gamma + ^7Be & \longrightarrow \beta + ^7Li^b \\
^7Be + p & \longleftrightarrow & \gamma + ^8B & \longrightarrow \beta + \otimes \\
^7Be + \alpha & \longrightarrow & \gamma + ^{11}C & \longrightarrow \beta + ^{11}B \\
^{11}C + p & \longleftrightarrow & \gamma + ^{12}N & \longrightarrow \beta + \otimes \\
^{11}B + p & \longrightarrow & \otimes & \\
^{11}C + \alpha & \longrightarrow & \otimes &
\end{array}
$$

[a] A $\otimes$ indicates that the reaction *products* are not accounted for in our reaction network. E. g. any production of ^4He would be insignificant given the enormous amounts of it already present, so any reaction which produces only ^4He enters only as a destruction reaction.

[b] β refers to any nuclear process involving electrons. The electron capture rate for $^7Be + e^- \longrightarrow ^7Li$ is so slow $\tau_{1/2} \sim 49$ days that we set it to zero in the actual equations.

TABLE 4

Piston name	source energy ($10^{51} ergs$)	kinetic energy	kinetic energy (% error)	^{7}Li (solar masses)	^{11}B
line	1.50076	0.45983	8.5942	3.8427e-10	3.0647e-18
correct	1.44345	0.41938	9.4794	3.6502e-10	3.2578e-18
flawed	1.74107	0.32704	12.668	2.5151e-10	3.4536e-16

TABLE 5

T_0 (keV)	ρ_0 (g/cm^3)	v_{shock} (10^8 cm/s)	v_1 (10^8 cm/s)			T_1 (keV)		
			analytical	numerical	% difference	analytical	numerical	% difference
0.1	0.01	1.285	1.012	1.005	0.69	0.992	0.968	2.44
		6.185	5.255	4.969	5.59	2.845	2.650	7.09
		11.98	10.24	9.408	8.46	4.039	3.110	25.9
		23.02	19.70	18.39	6.87	5.640	5.477	2.93
1.0	0.1	1.466	1.007	1.013	0.59	1.882	1.890	0.42
		6.341	5.333	5.074	4.97	5.021	4.611	8.51
		12.42	10.58	9.935	6.28	7.256	6.195	15.7
		23.68	20.25	19.22	5.21	10.14	9.792	3.49
1.0	1.0	1.371	8.880	10.07	12.5	2.352	2.124	10.1
		6.330	5.275	5.089	3.58	8.569	7.725	10.3
		12.57	10.67	10.10	5.48	12.80	11.27	12.7
		26.19	22.38	19.67	12.8	18.89	17.64	6.84
5.0	5.0	2.244	1.103	1.022	7.62	6.403	6.515	1.73
		6.640	5.330	5.105	4.31	12.89	13.94	7.82
		12.85	10.75	10.12	6.03	19.07	18.01	5.71
		28.54	24.32	20.02	19.3	29.39	26.97	8.58
		36.40	31.08	28.88	7.33	33.34	32.47	2.64

TABLE 6

Model name	source energy ($10^{51} ergs$)	kinetic energy	kinetic energy (% error)	simulation seconds[a]	^{7}Li (solar masses)	^{11}B
m150	0.29385	0.15486	15.855	1000	3.2158e-12	1.2333e-22
	0.97105	0.37325	10.219	1000	1.9340e-11	7.3619e-19
	2.18326	0.72148	9.2790	1000	5.6805e-11	4.2014e-17
	3.87165	1.12993	9.2871	1000	1.1455e-10	4.7348e-16
m151	0.34535	0.31627	6.9998	1000	1.6752e-14	9.2134e-29
	1.38906	1.14966	6.4274	1000	4.5096e-13	1.6257e-24
	2.89712	2.25534	6.4601	1000	1.8693e-12	1.2783e-22
	3.53510	2.65417	4.6897	1000	3.2910e-12	1.3568e-21
m152	0.33863	0.30640	7.5224	1000	8.5421e-14	6.3490e-28
	1.32960	1.08162	6.9534	1000	2.1383e-12	8.4426e-24
	3.02116	2.30563	6.4905	1000	8.6564e-12	6.1905e-22
	3.75584	2.69552	4.9383	1000	1.5630e-11	6.6912e-21
m251	0.30519	0.10868	38.051	1000	2.0853e-11	1.0467e-22
	1.24211	0.28112	20.664	1000	2.5416e-10	7.2309e-19
	2.76511	0.50675	15.343	1000	8.9687e-10	6.5810e-17
	4.13690	0.63388	14.100	1000	1.7477e-09	6.2910e-16
	6.64756	1.50023	6.051	147	3.3559e-09	3.7072e-15
	9.12673	1.95884	5.715	130	4.9402e-09	1.3272e-14
m252	0.24754	0.10225	38.803	1000	1.2461e-11	6.8521e-25
	0.99500	0.25737	20.814	1000	1.5904e-10	5.8135e-22
	2.20954	0.46378	15.024	1000	5.8167e-10	7.3852e-20
	3.46763	0.60426	13.313	1000	1.1651e-09	2.2900e-18
o100	0.61285	0.50398	19.1328	200	8.2099e-12	6.4412e-27
	2.81542	1.99089	6.2674	100	1.0315e-10	8.4875e-24
	5.57902	3.44104	5.6527	150	3.1250e-10	2.8680e-22
	9.74379	5.62623	4.9346	150	6.6917e-10	2.8020e-21
o58	0.93739	0.18375	179	700	1.4003e-13	1.08214e-27
	3.10352	1.87221	28.2923	650	1.8622e-12	9.9448e-26
	16.0503	7.49521	7.4246	350	3.9765e-11	4.6342e-23

[a] Energetics errors tend to grow with time.

FIGURE 1

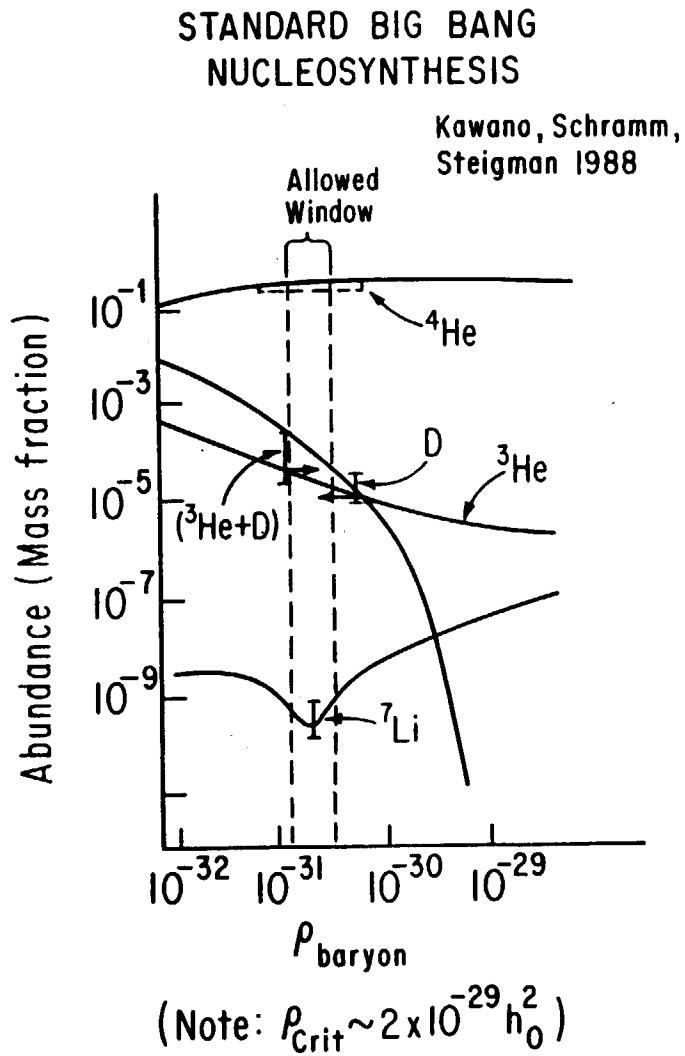

FIGURE 2

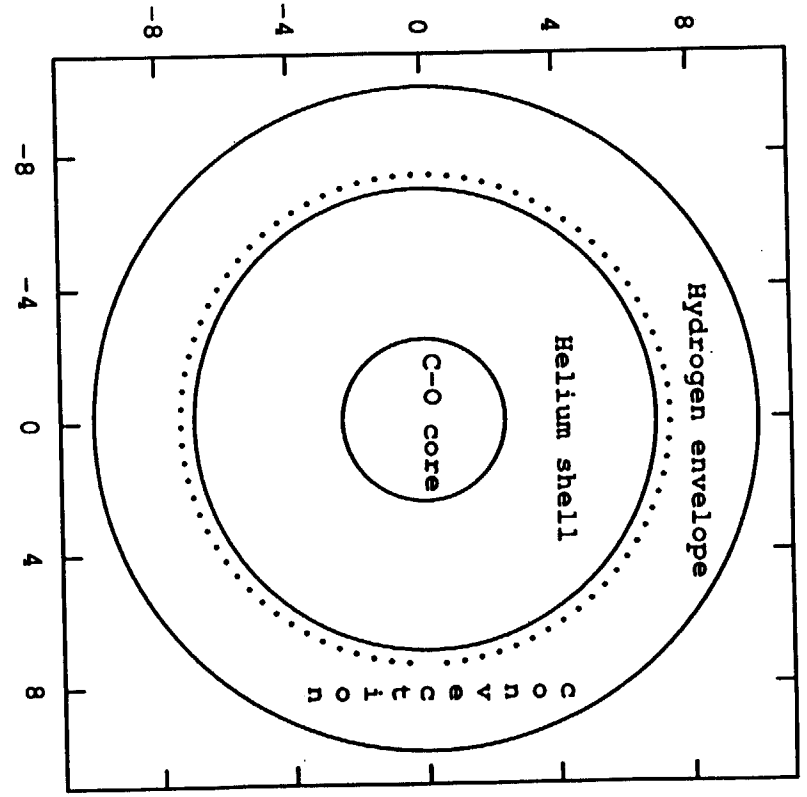

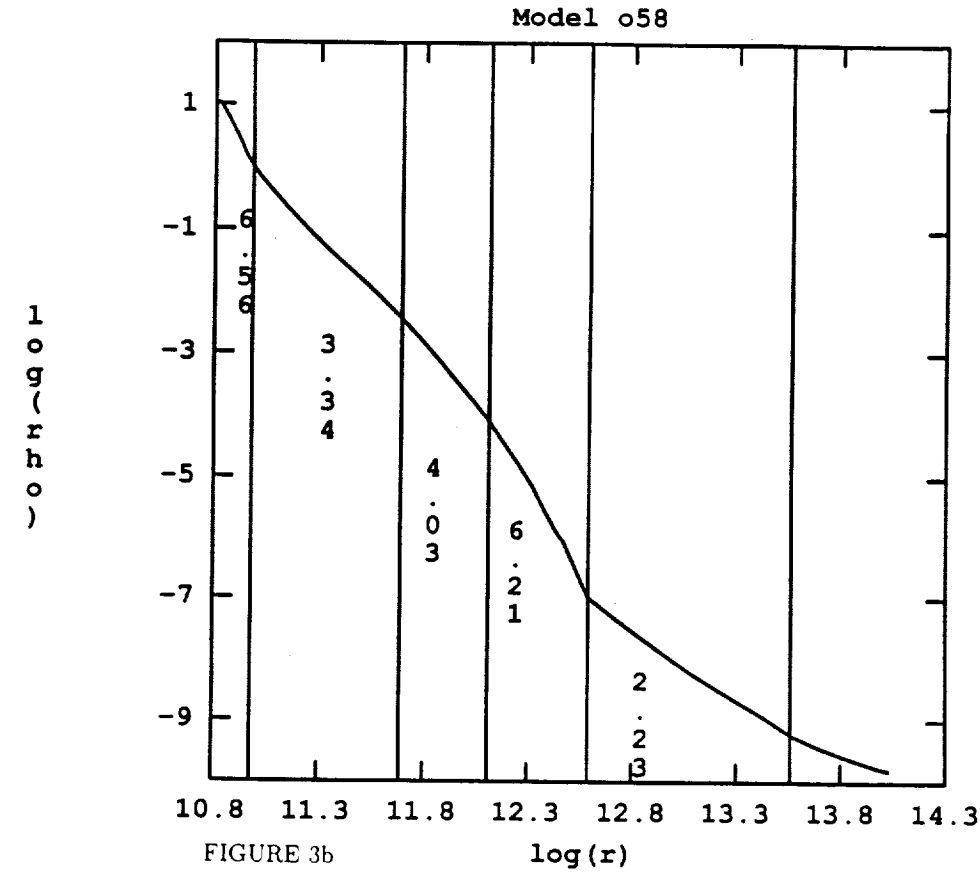

FIGURE 3b

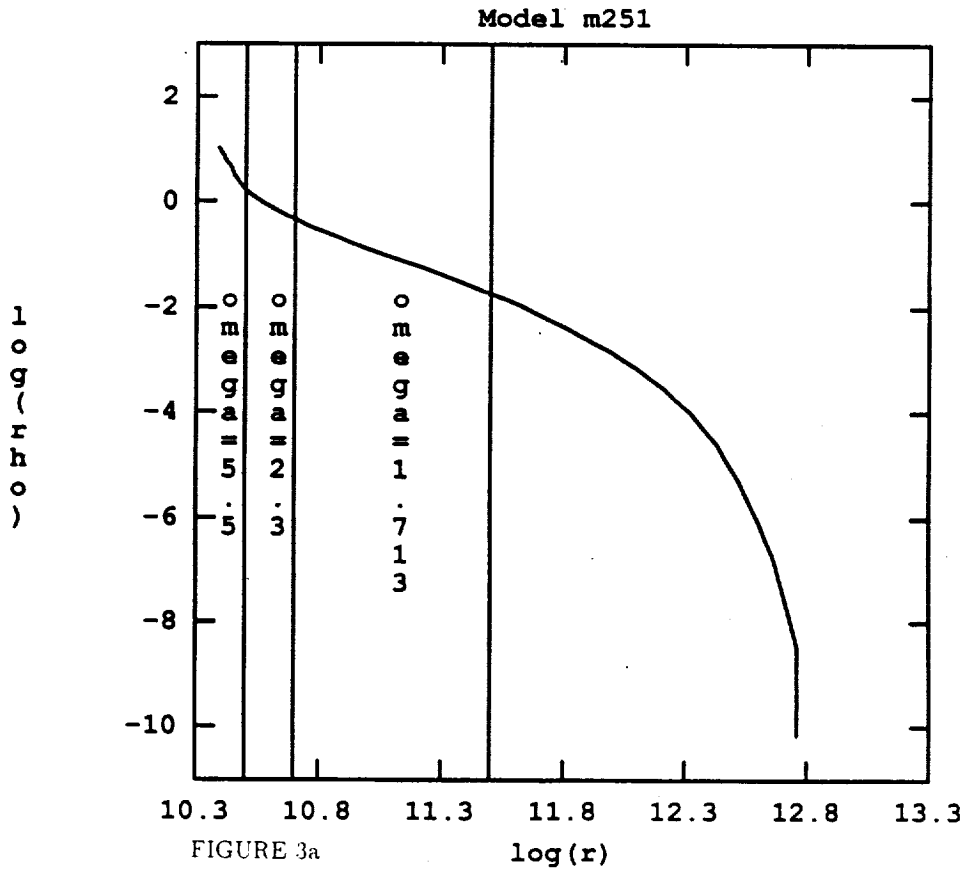

FIGURE 3a

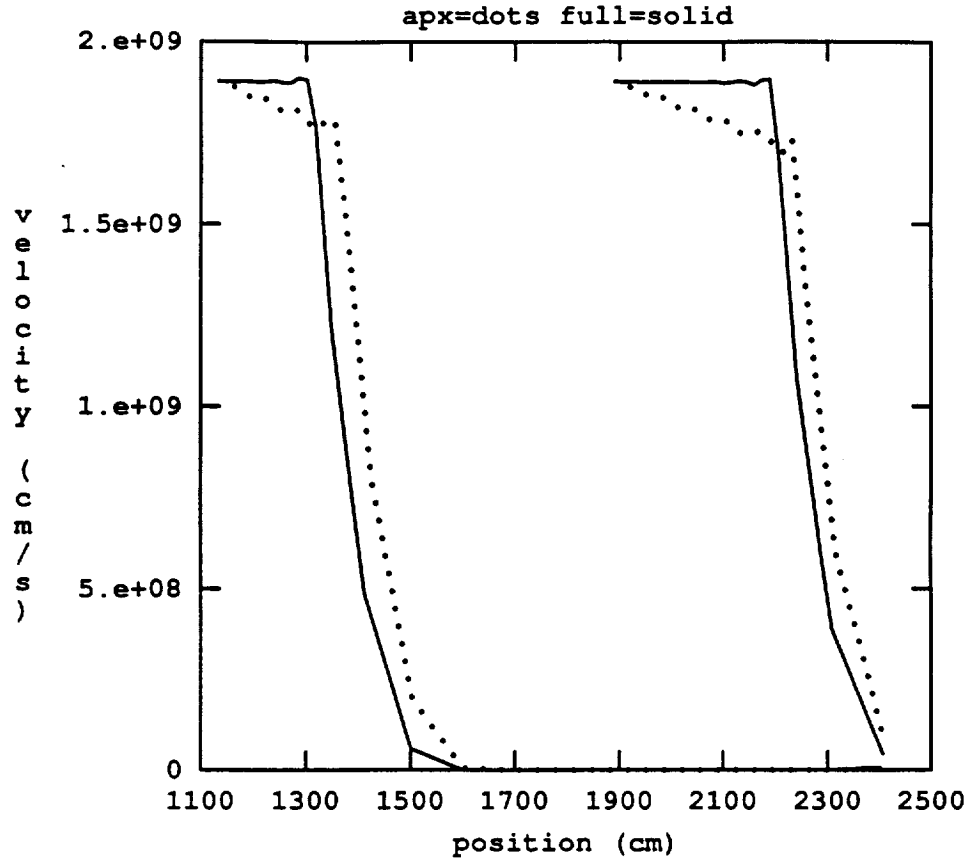

FIGURE 5

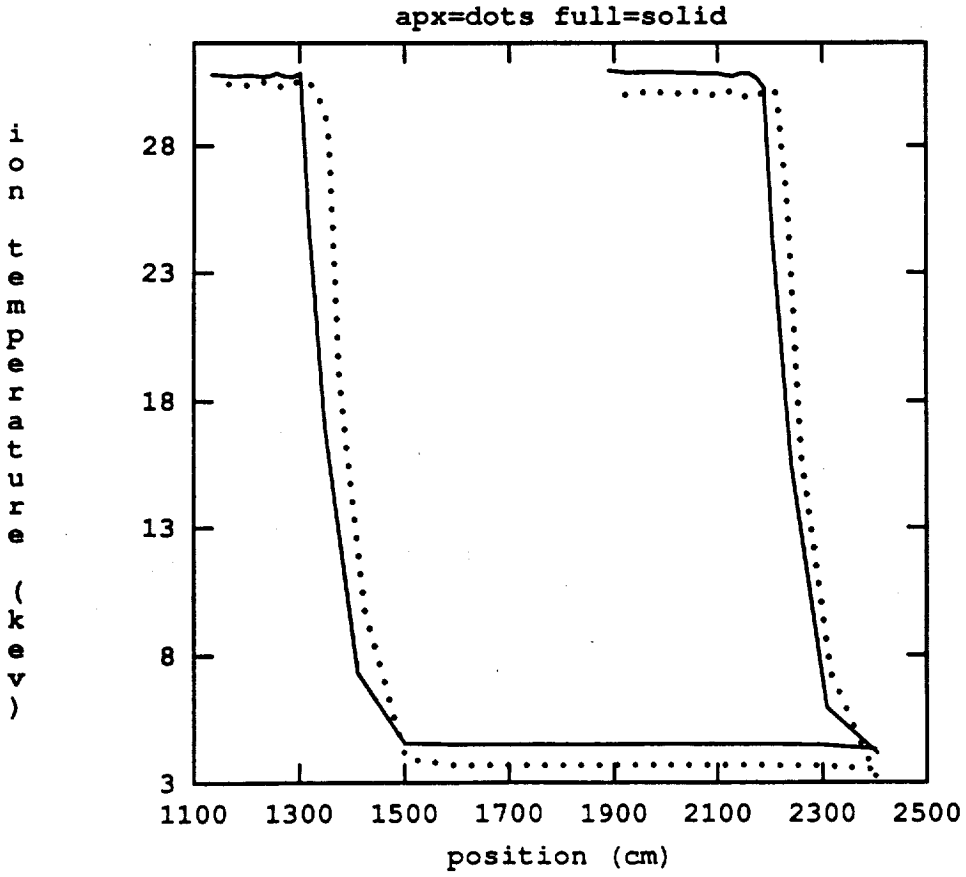

FIGURE 4

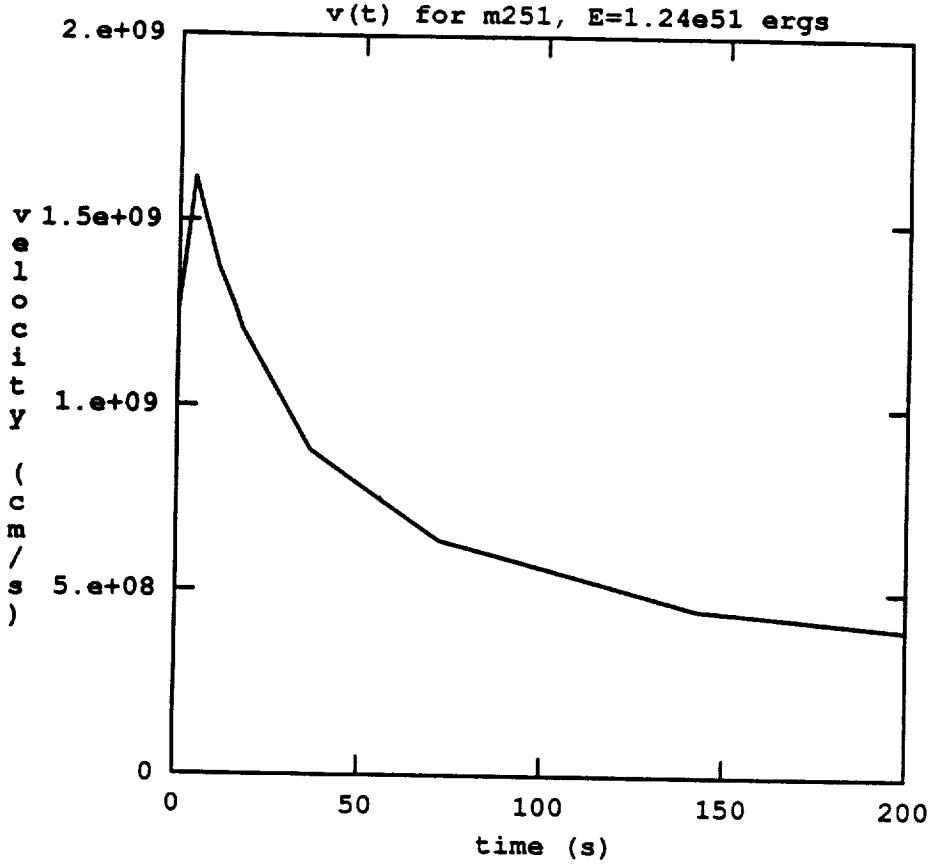

FIGURE 7

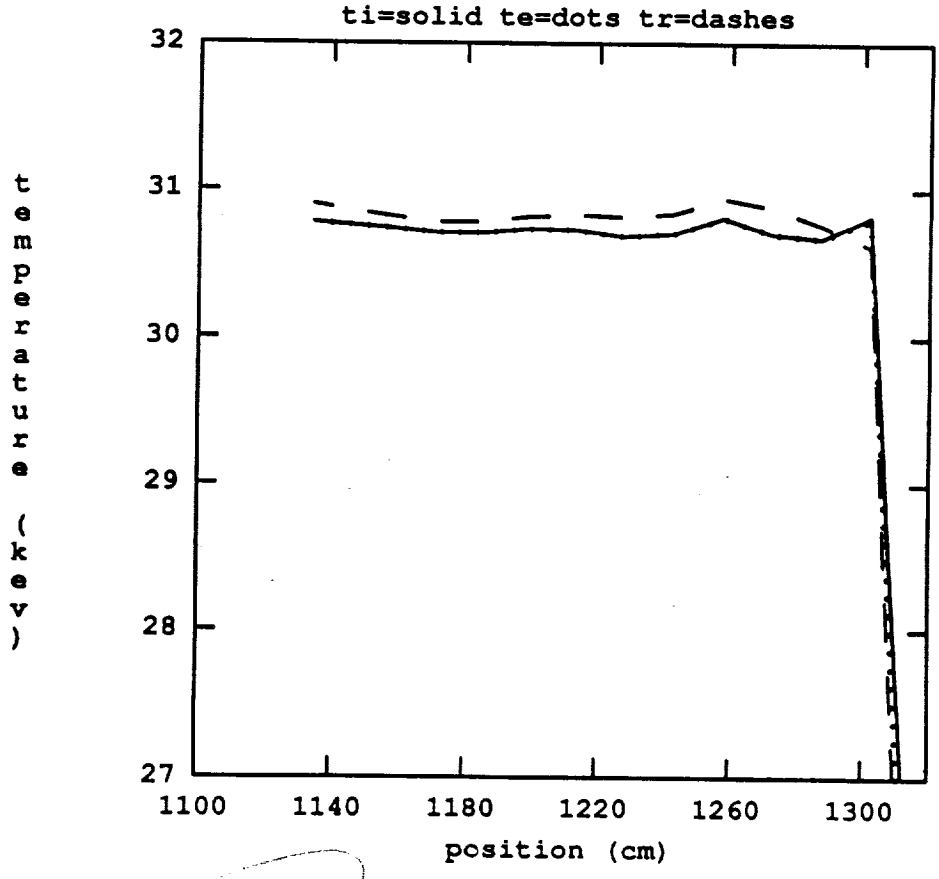

FIGURE 6

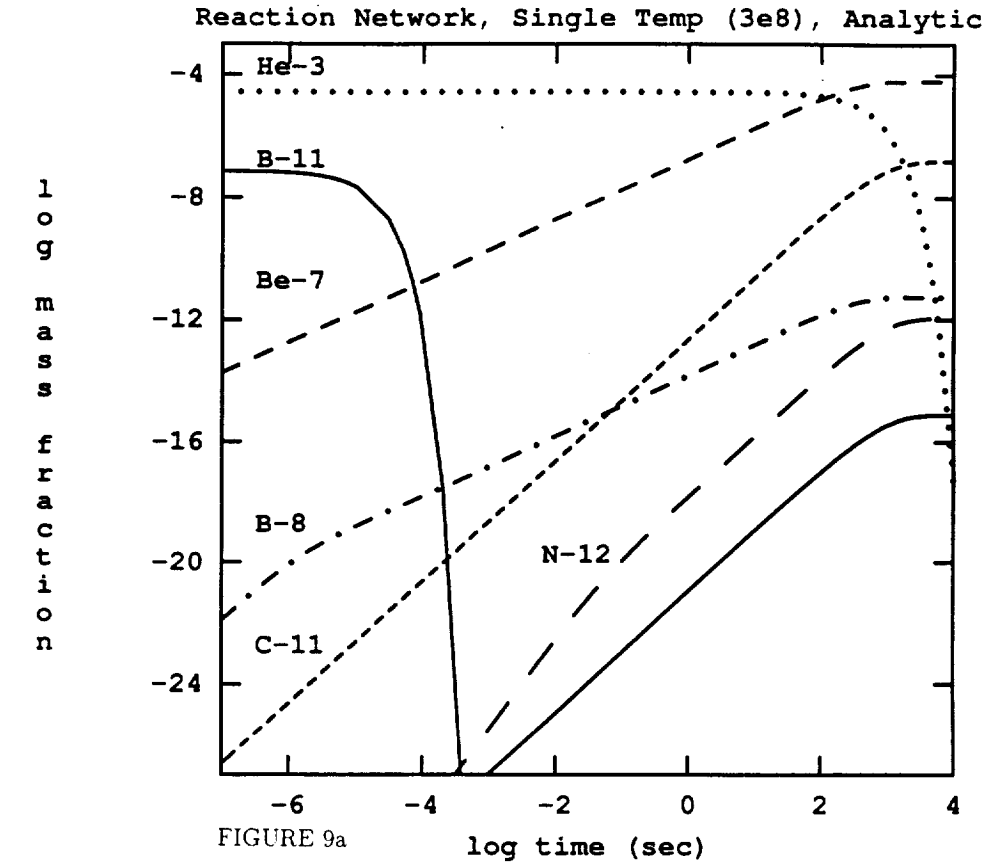

FIGURE 9a

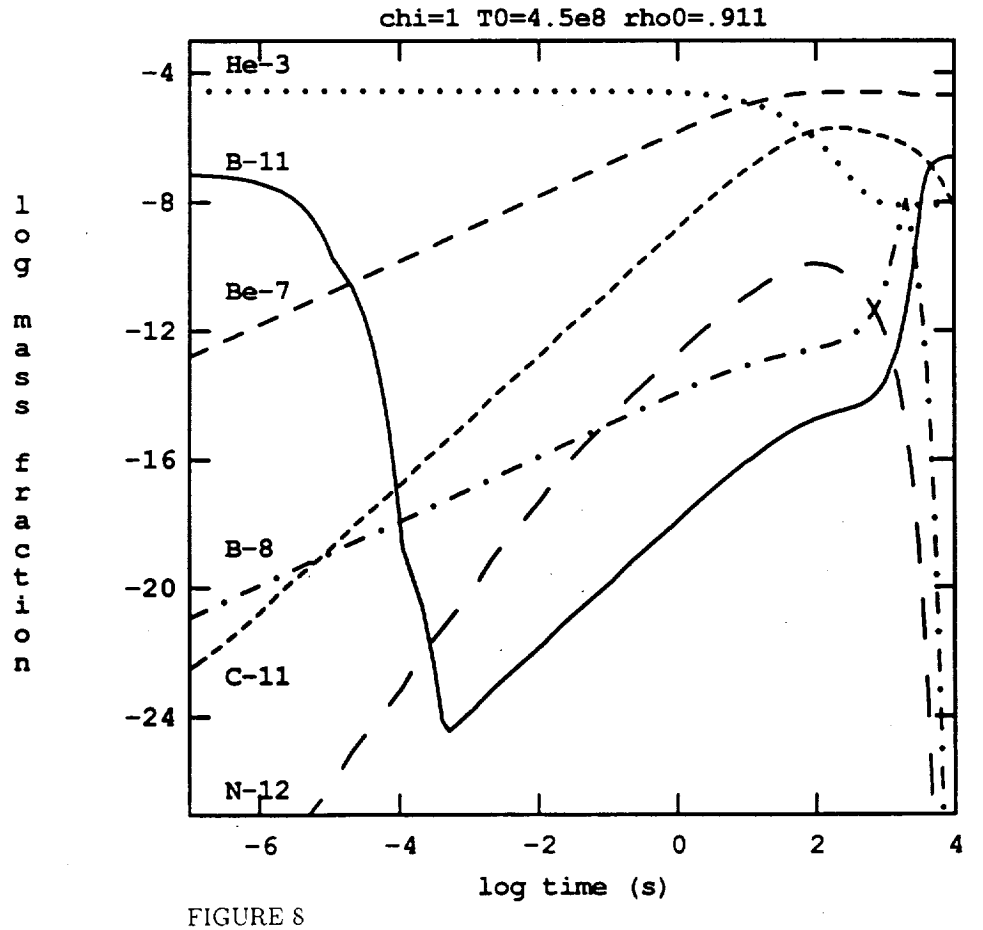

FIGURE 8

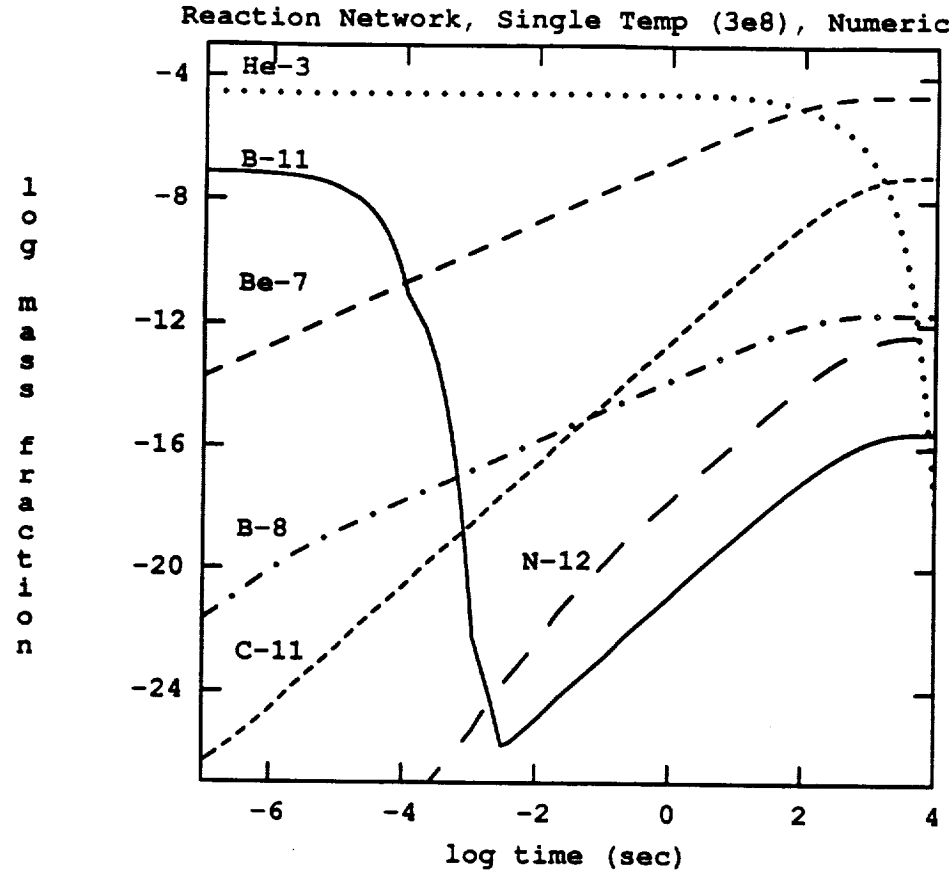

FIGURE 10

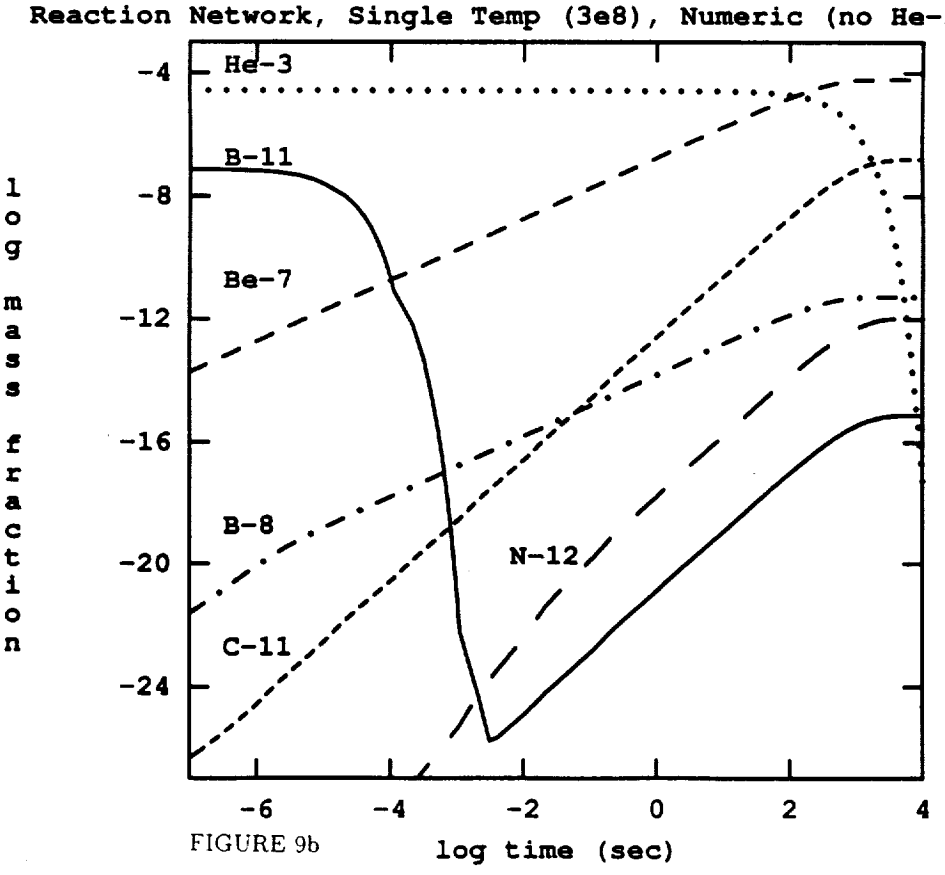

FIGURE 9b

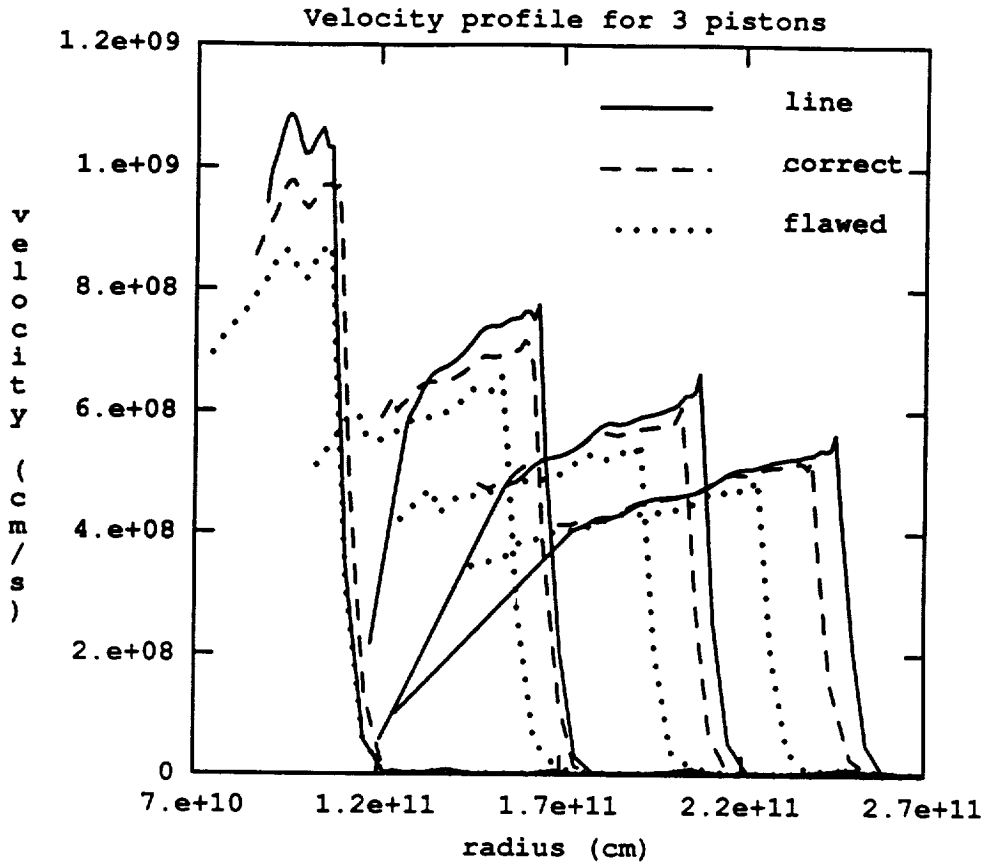

FIGURE 12

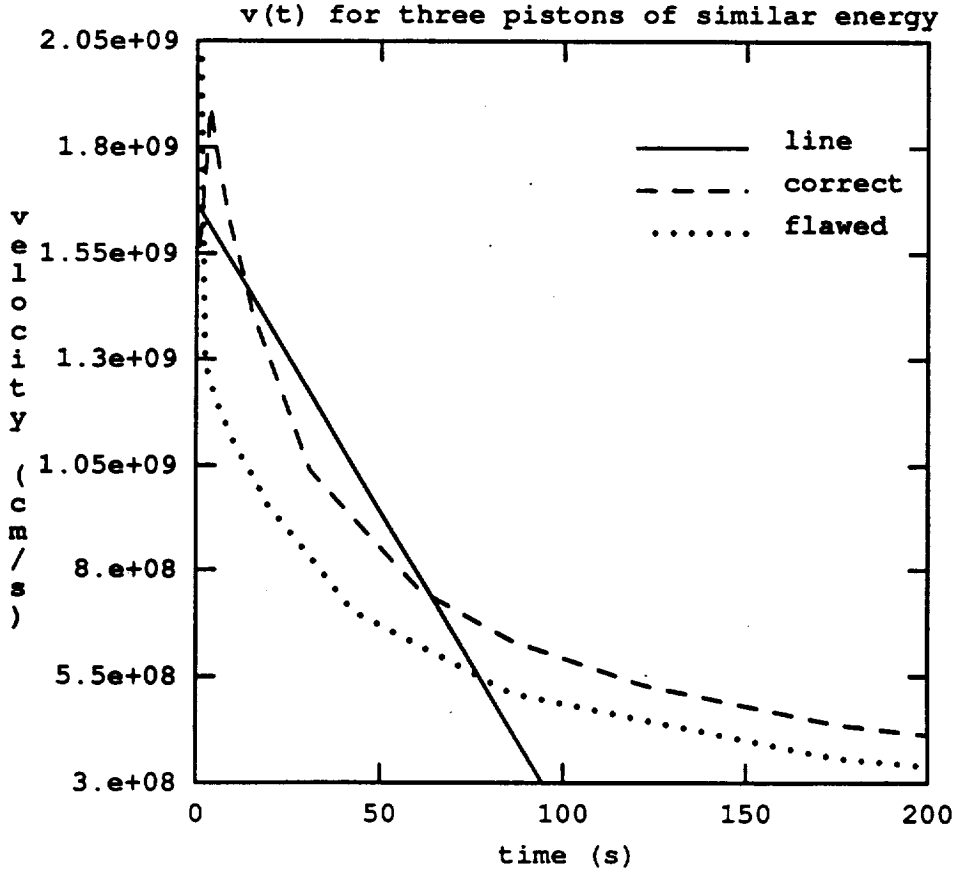

FIGURE 11

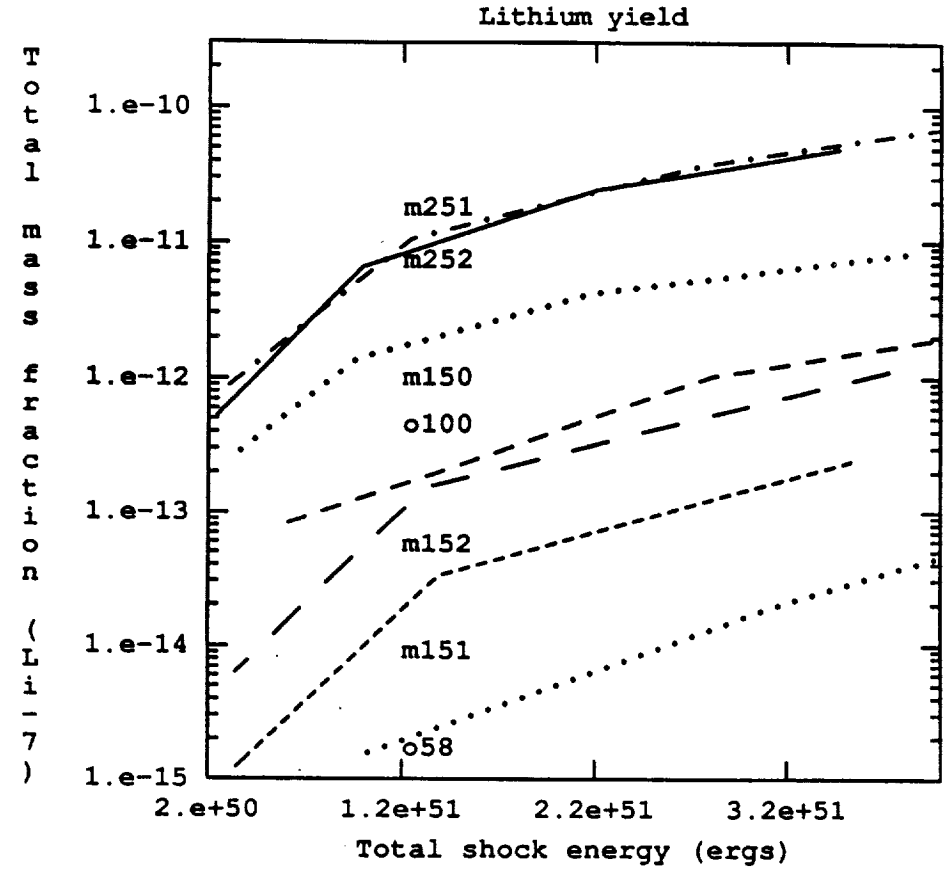

FIGURE 14

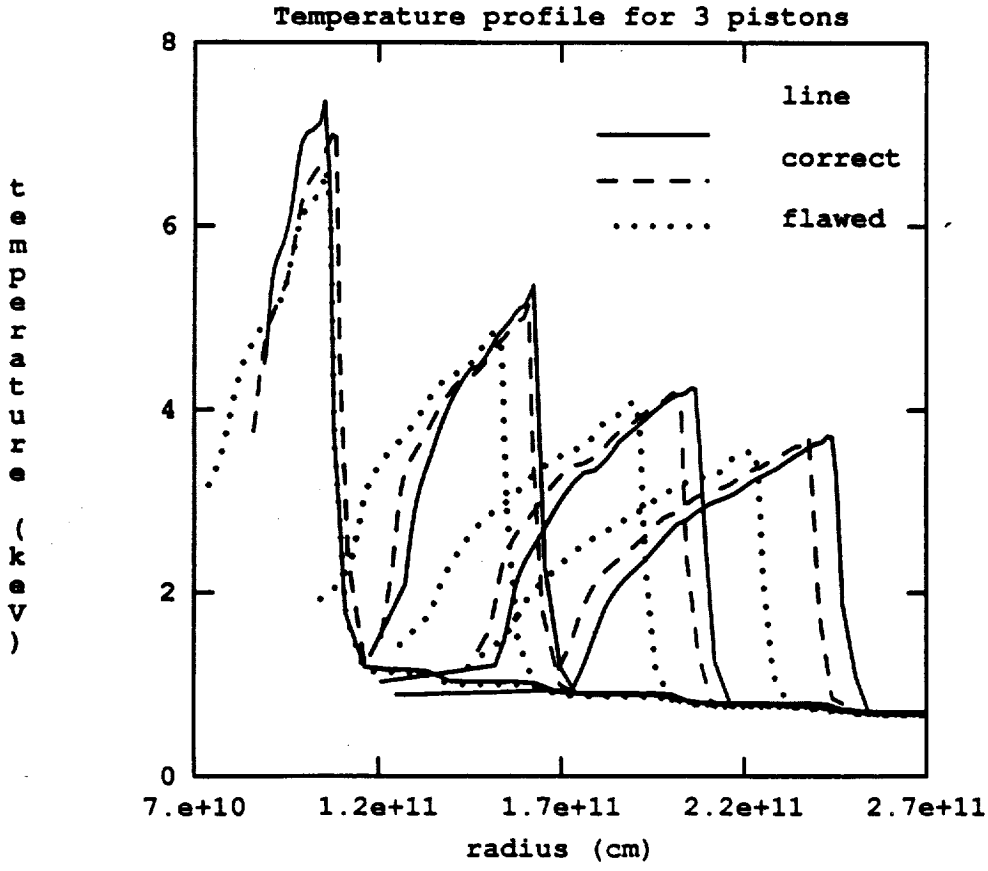

FIGURE 13

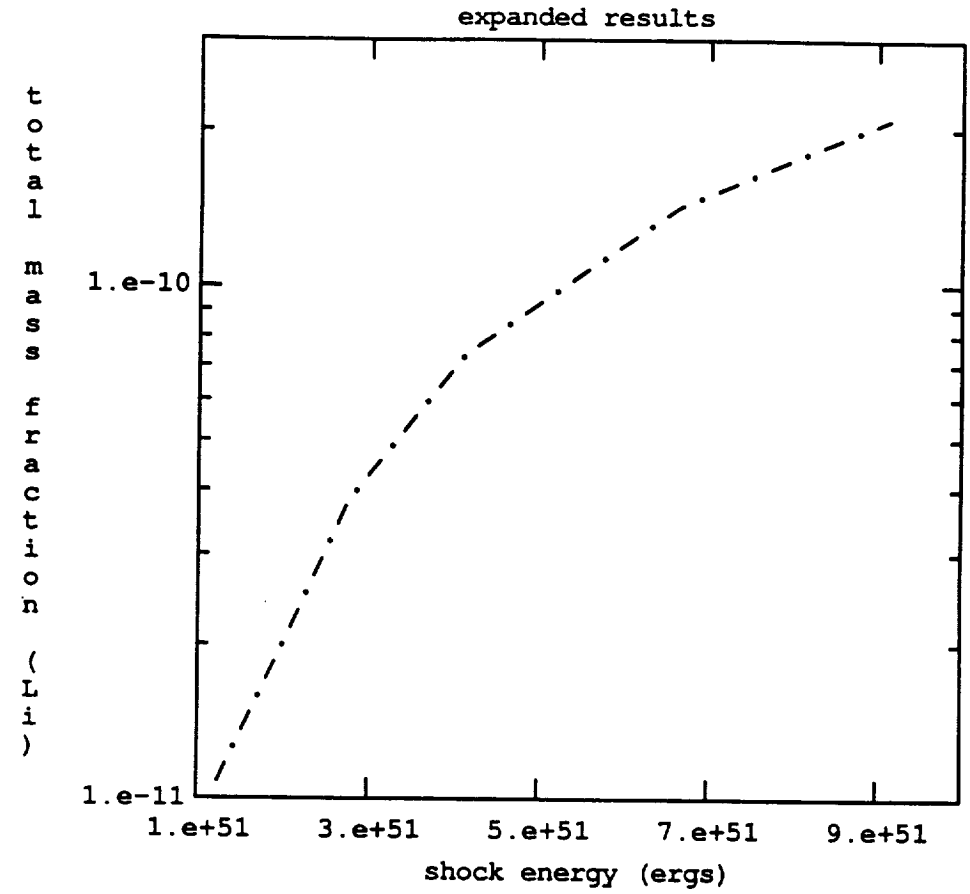

FIGURE 16

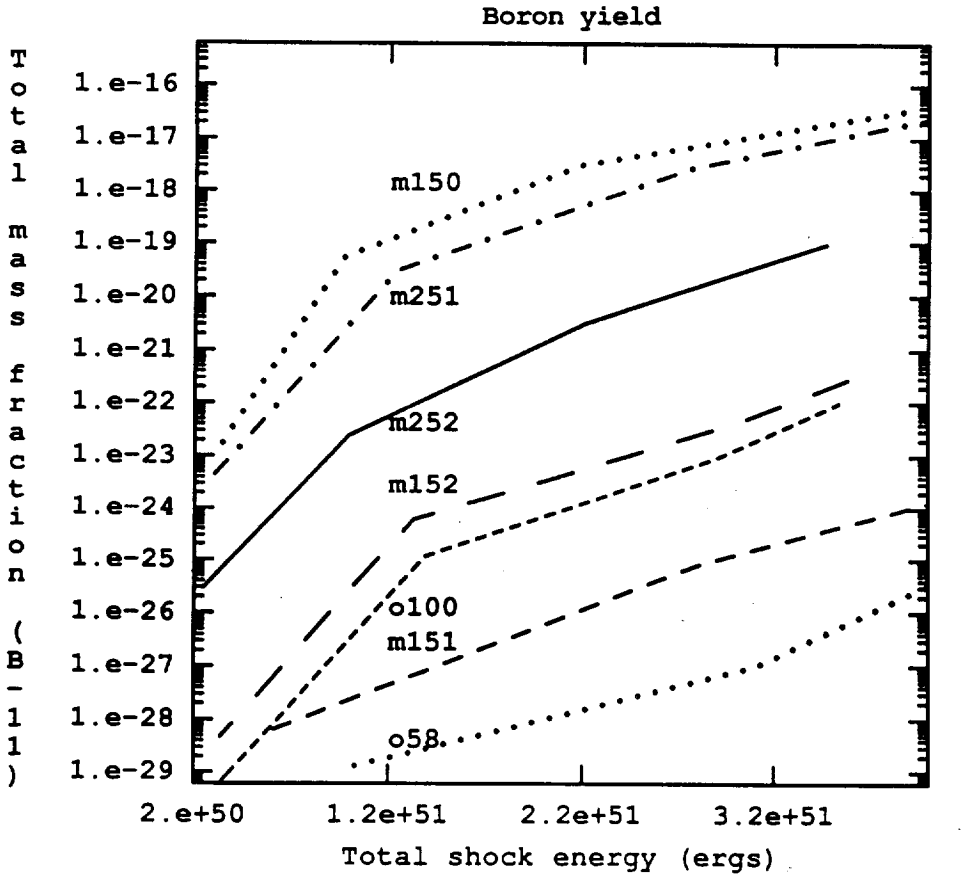

FIGURE 15

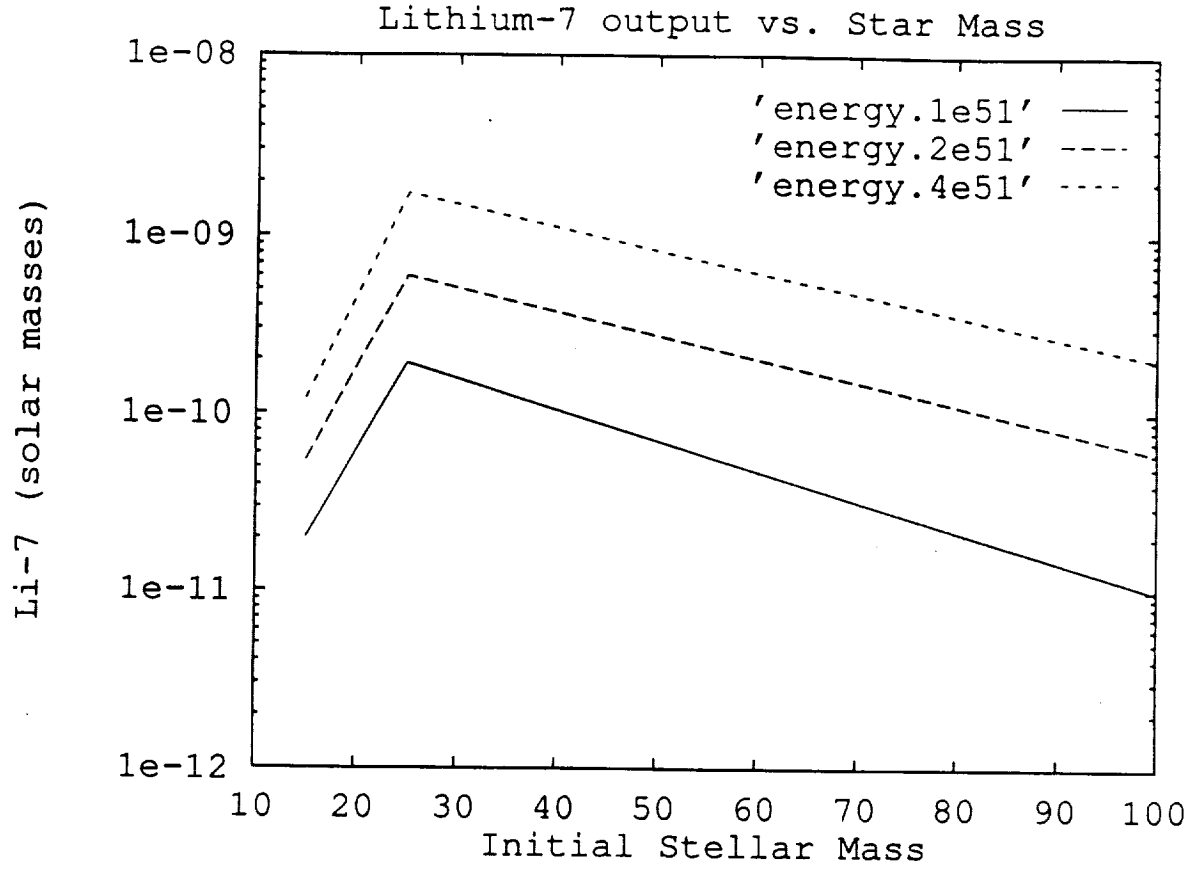

FIGURE 18

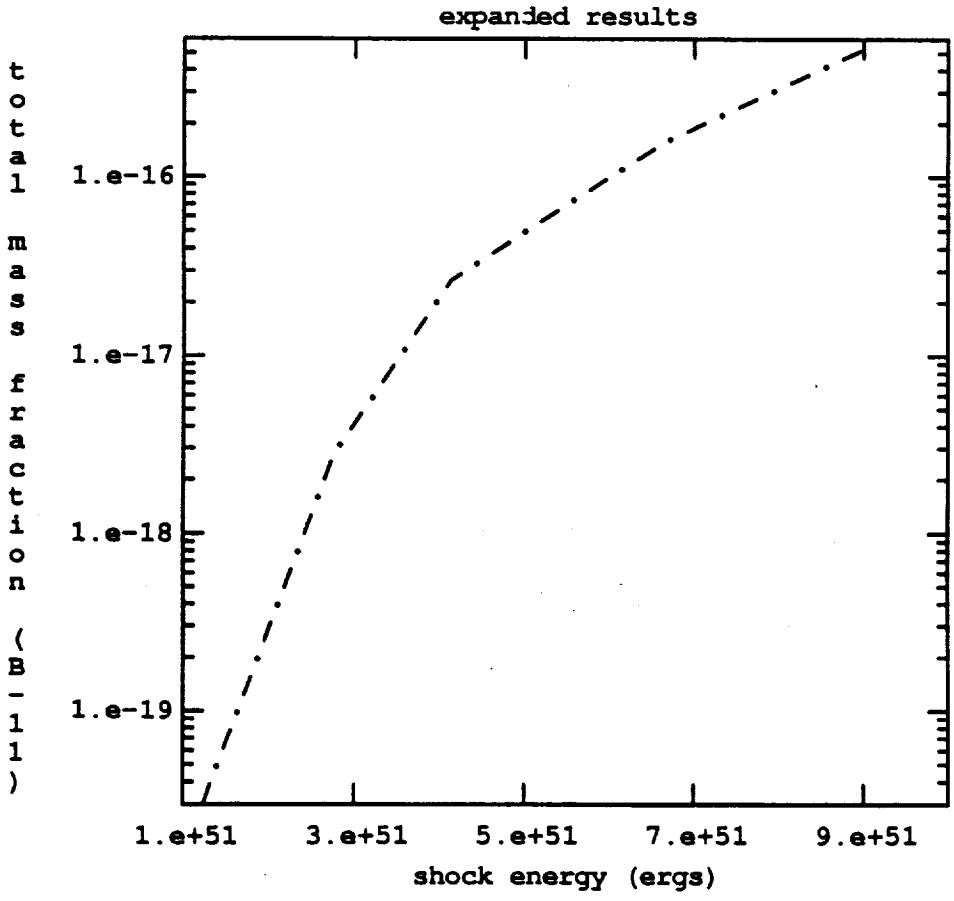

FIGURE 17

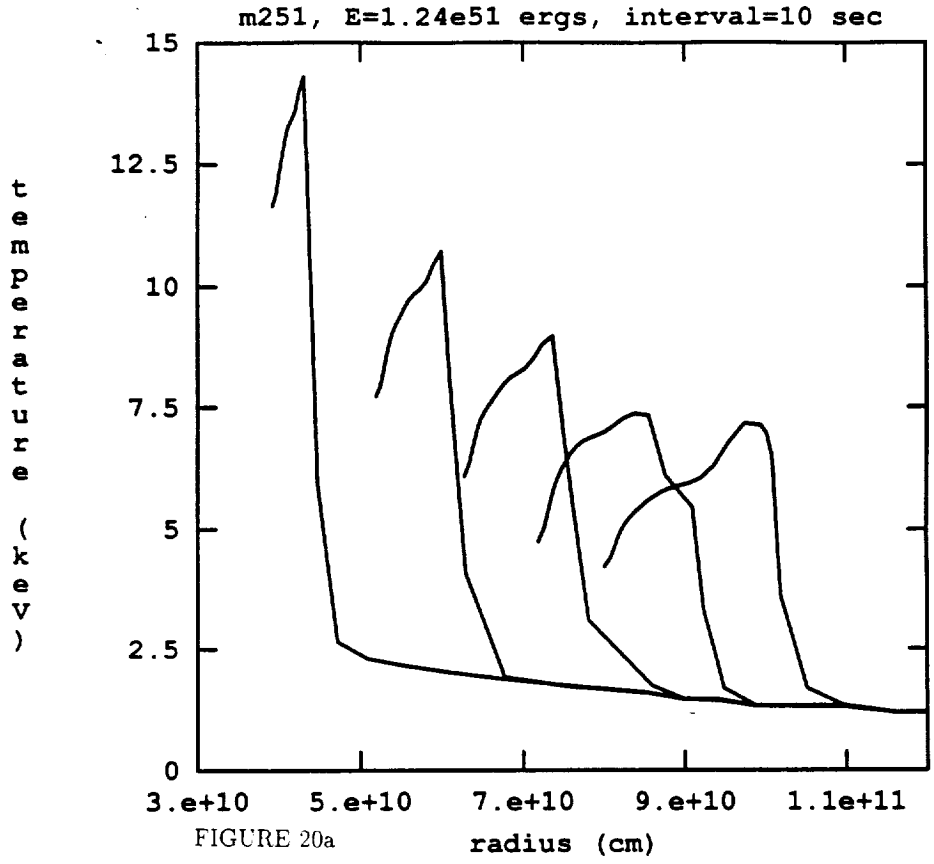

FIGURE 20a

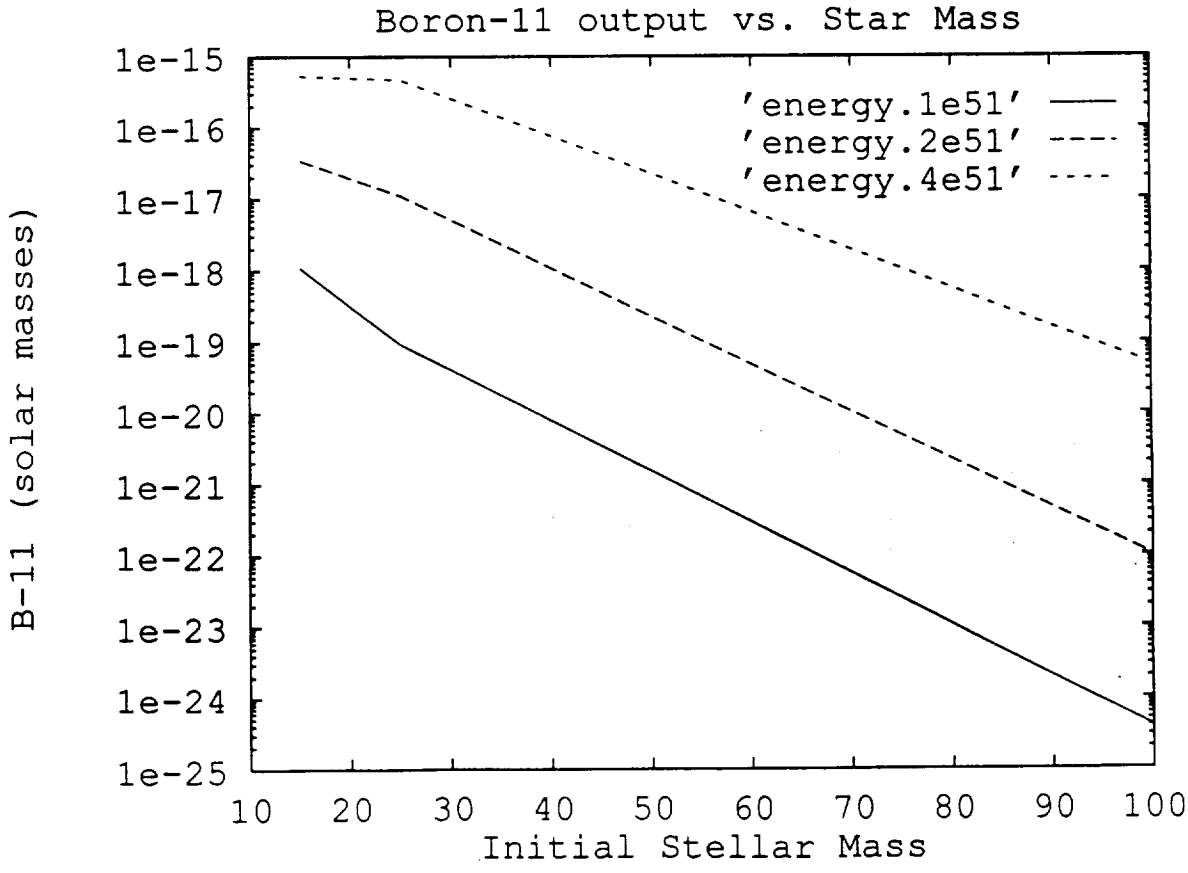

FIGURE 19

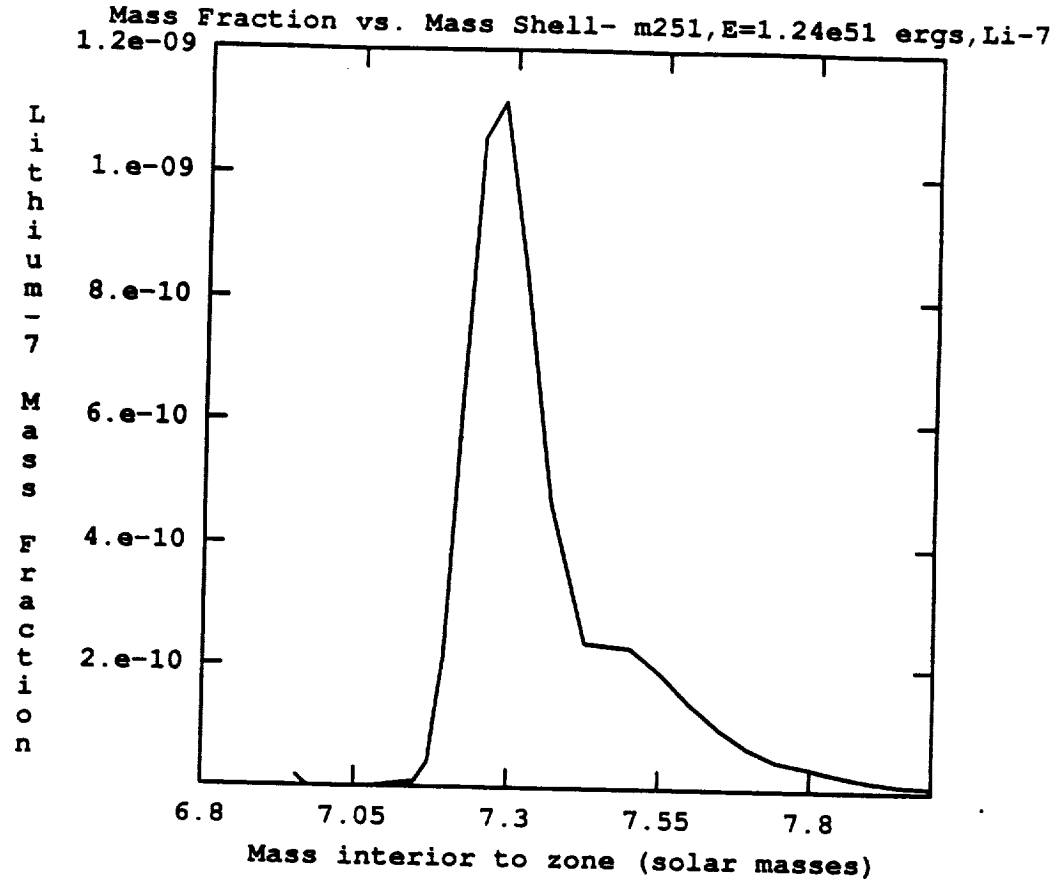

FIGURE 21

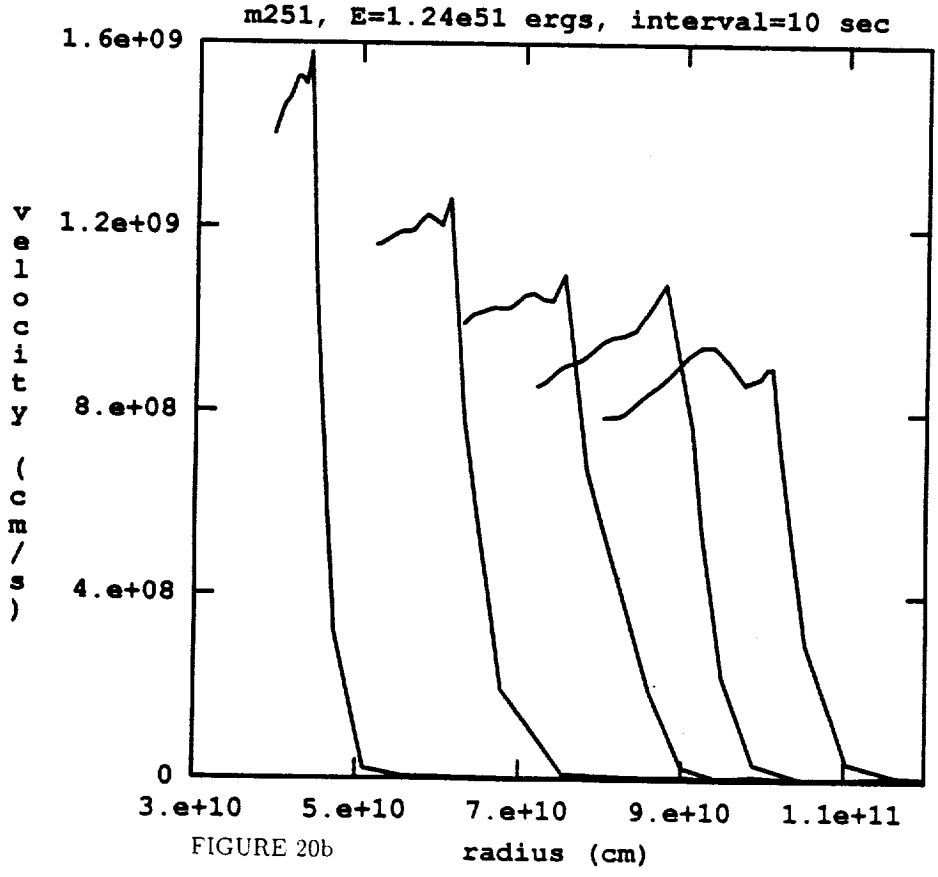

FIGURE 20b

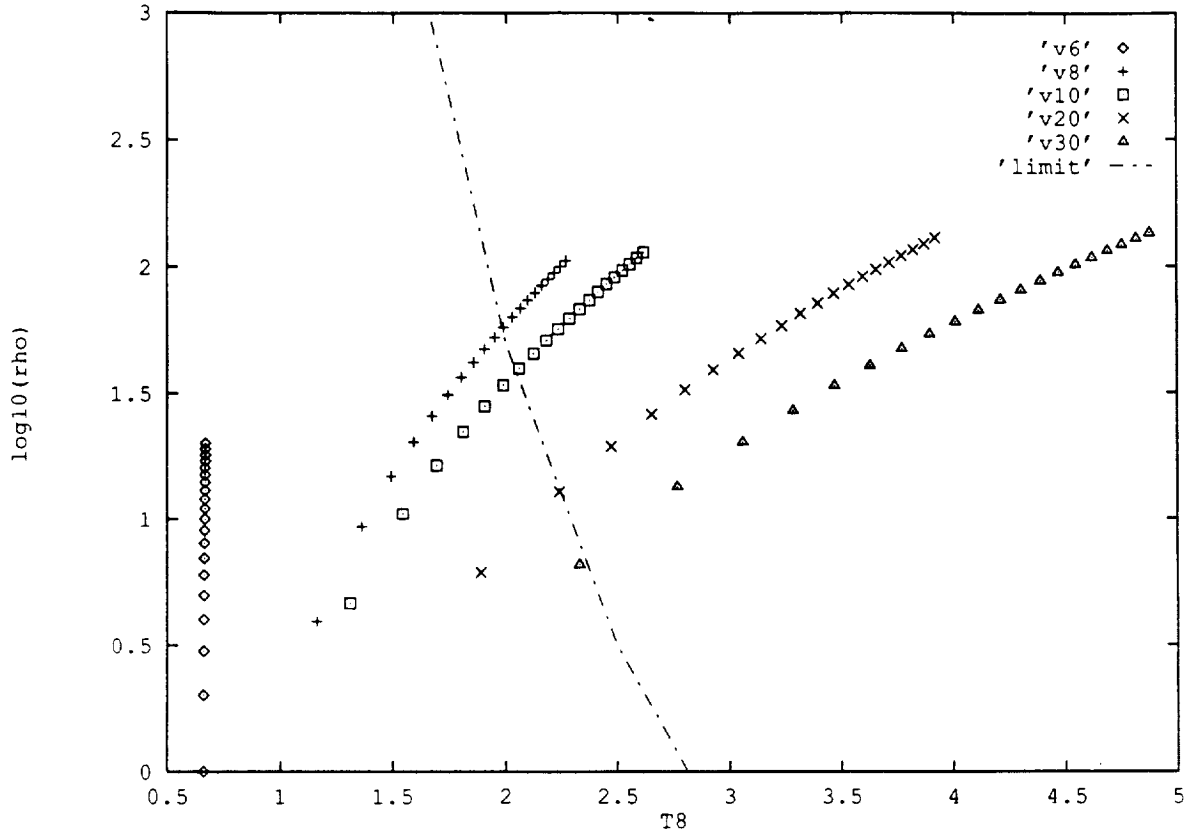

FIGURE 23

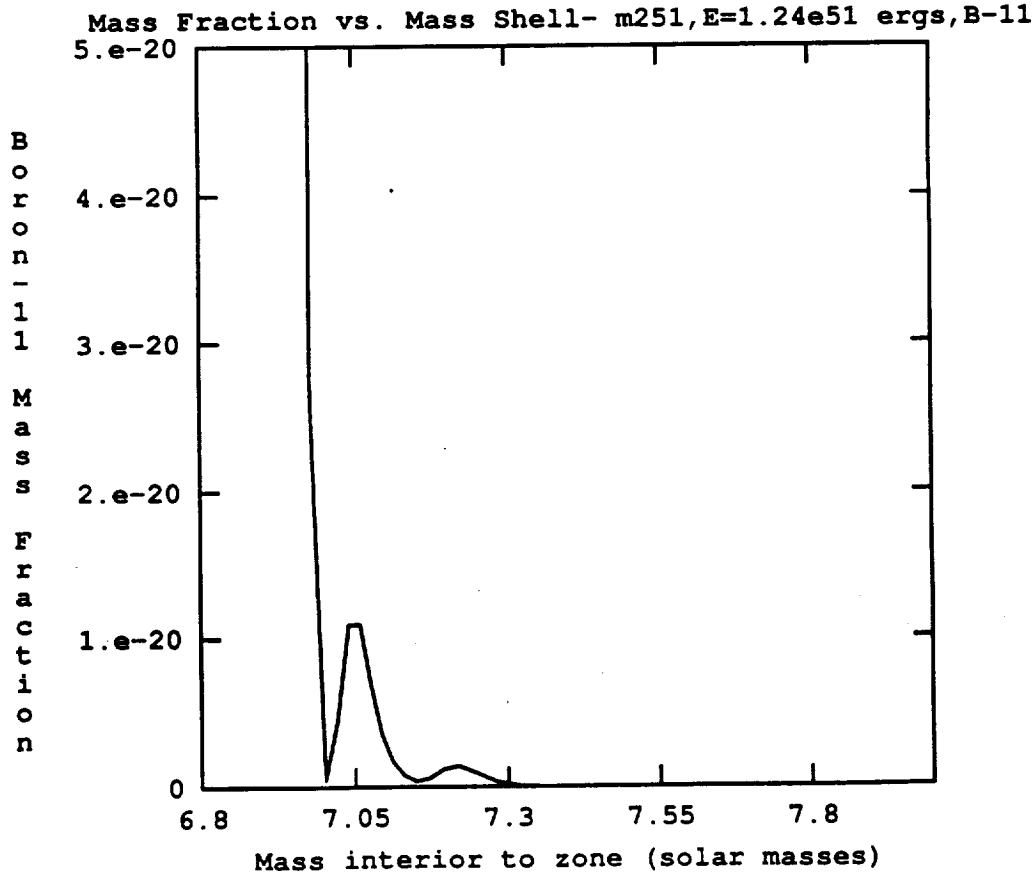

FIGURE 22